Chapter 6: On a Bio-Inspired Method for Topology Optimization via Map L-Systems and Fractone Modeling

Chapter details

Chapter DOI:

https://doi.org/10.4322/978-65-86503-71-5.c06

Chapter suggested citation / reference style:

Kobayashi, Marcelo H. (2022). “On a Bio-Inspired Method for Topology Optimization via Map L-Systems and Fractone Modeling”. *In* Jorge, Ariosto B., et al. (Eds.) *Model-Based and Signal-Based Inverse Methods*, Vol. I, UnB, Brasilia, DF, Brazil, pp. 237–268. Book series in Discrete Models, Inverse Methods, & Uncertainty Modeling in Structural Integrity.

P.S.: DOI may be included at the end of citation, for completeness.

Book details

Book: Model-based and Signal-Based Inverse Methods

Edited by: Jorge, Ariosto B., Anflor, Carla T. M., Gomes, Guilherme F., & Carneiro, Sergio H. S.

Volume I of Book Series in:

Discrete Models, Inverse Methods, & Uncertainty Modeling in Structural Integrity

Published by: UnB City: Brasilia, DF, Brazil Year: 2022

DOI: https://doi.org/10.4322/978-65-86503-71-5

On a Bio-Inspired Method for Topology Optimization via Map L-Systems and Fractone Modeling

Marcelo H. Kobayashi[1]

[1]University of Hawaii at Manoa, Department of Mechanical Engineering, 2540 Dole Street–Holmes Hall 302, Honolulu, HI 96822. Email: marcelok@hawaii.edu

Abstract

Nature has long been a source of inspiration to both engineers and designers alike. This chapter describes a bio-inspired, topology optimization method for engineering design optimization. The method is based on evolutionary developmental processes in biology and employs a cellular division model to develop topologies. Concretely, a Map L-System, a graph based, parallel rewriting method, is used to model the cellular division process that generates the topology of the design, and a genetic algorithm is then used to evolve a population of designs. In the developmental process of the structure, fractones, elements that play a fundamental role in the regulation of cellular divisions, are modeled and incorporated as an additional control parameter for the formation and optimization of topologies. The performance of the resulting method is illustrated with an aeroelastic flapping membrane wing optimization problem in which the supporting structure is optimized for power, lift, and thrust requirements.

1 Introduction

Topology optimization seeks the economical distribution of material within a design domain, while satisfying a set of constraints. There exists myriad computational methods for topology optimization, each employing a variety of techniques and with unique advantages as well as limitations—see the monographs Rozvany [1994], Allaire [2002], Bendsøe and Sigmund [2003], Osher and Fedkiw [2003] and review papers Gain and Paulino [2013], van Dijk et al. [2013], Deaton and Grandhi [2014], Wang et al. [2021] for a detailed description and study of the existing methods.

The most popular method for topology optimization, namely, the solid isotropic material with penalization (SIMP), involves a "pixelation" of the design domain. The color of each pixel is determined by a density function, ρ, that can vary from zero (void) to one (solid). The addition of non-physical "gray" material ($0 < \rho < 1$) is penalized by raising the density function to a power $p \in \mathbb{N}, p > 1$, and defining the stiffness tensor at a point as the product $\rho^p E_0$, where E_0 is the elasticity tensor of the structural material. Since ρ^p, the addition of gray material is made less effective as p increases, thus reducing the regions with gray material in the domain. Though simple to implement and intuitive in its formulation, the designs obtained with SIMP require post-processing to interpret the optimized layout, since inevitably they contain regions of artificial, gray material. In addition, filtering techniques and high resolution are often required to achieve meaningful results from these methods—higher resolution in turn greatly increases the computational demand to explore the design domain. To alleviate these demands, a genetic algorithm (GA) may be employed. In this approach complex problems may converge toward optimal designs without exploring every possibility, by directly translating the discretized domain into a genome and simulating a natural selection process to evolve the topologies. In addition, given the independence of the individuals in the population, perfectly parallelizable algorithms can be easily devised to speed up the computation of the population of designs in each generation.

The biologically inspired method described in this chapter takes advantage of the evolutionary algorithm, but it generates topologies without a discretization of the domain, thus avoiding the mesh dependency of the results that arise from the pixelation resolution. In place of a pixelated approach, the map L-system follows the sequence of rules to generate a vast pool of maps, which can be translated into engineering structures.

Previous studies have proven this biologically inspired method capable of successfully performing complex optimizations—see, for instance, Kobayashi et al. [2009], Stanford et al. [2012], Stanford et al. [2012], Kolonay and Kobayashi [2015]. Here we explore a mechanism of cellular division in neurosciences to enhance the search effectiveness and efficiency in discovering and refining of optimized solutions to engineering problems.

2 Map L-Systems

Introduced in 1968 by biologist Aristid Lindenmayer, the Lindenmayer system (or L-system) is a method of rewriting a series of character/grammar strings in a parallel fashion. The versatility of the L-system to represent the parameters of any starting element with a character string and evolve the structure by implementation of the governing production rules has proven the system to be useful for a number of applications. Some applications include the ability to produce interesting fractal geometries, model the branching growth of plant structures, and simulate cellular divisions—see figure 1. The map L-system proposed by Nakamura, Lindenmayer, and Aizawa (Prusinkiewicz and Lindenmayer [2004] Nakamura et al. [1986]) is an extension of L-systems for graphs that are maps, and was originally develop

to model single layer cellular divisions. This class of methods forms the basis for modeling the topologies of structures in this work.

Maps are planar graphs defined by a finite set of regions in which each region is enclosed by a string of edges which meet at vertices. Every edge has one or two associated vertices, all edges are a part of a region's boundary, and all edges are connected (such that there are no 'islands' within the domain). A map may be representative of a single cellular layer where the edges are the cell wall, the enclosed regions are the intracellular space within the cells and the extracellular spaces lay within the walls. Simultaneous cell divisions are modeled with a binary propagating map 0L system with markers (or mBPM0L-system). The 0L system is the context-free Lindenmayer parallel rewriting system in which there are no interactions between cells. The map L-system is binary and propagating because cells are always divided into two daughter cells and in this model cells are never destroyed or joined. The markers play the functional role of flagging the boundary edges at potential vertices where the cell may divide and new edges may form (see Prusinkiewicz and Lindenmayer [2004]).

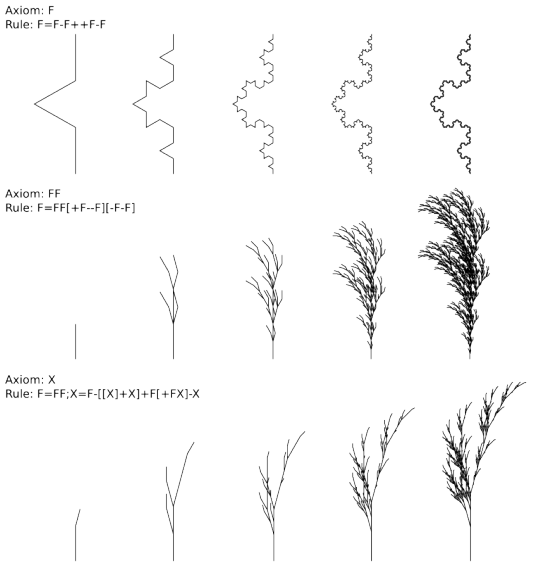

Figure 1: Sample images generated by L-systems: fractal pattern (top), development of plant structures (mid and bottom)

Informally, a two dimensional map L-system is first initiated with an axiom that defines the edges of the domain. Once initiated, the closed map undergoes a series of subdivisions by the addition of straight internal edges. The creation and location of these edges are governed by a predefined set of production rules. The algorithm begins each iteration with a discretization of the existing edges of the map and a placement of markers at selected nodes. The discretization patterns of the edges and the location and orientation of markers are based on the production rules. Once all edges have been divided and markers placed, the new edges are created by matching the markers. When two markers are present along the boundary of a common region, have the same label, and appropriate orientations, they will form a new wall between the two markers.

Mathematically, the system is defined by an alphabet, Σ, which is a finite set of characters (letters and symbols) and may be represented as $\Sigma = \{A, B, C, ..., [,], +, -\}$. From this alphabet, characters are selected to create an axiom, Ω, which is the string that initiates the rewriting process. For example, an axiom would be $\Omega = ABAB$. The third and final item required is the finite set of production rules or rewriting rules, P. The production rules are also limited to the characters of the alphabet, Σ, and must take the form $\alpha \rightarrow \chi$, where α is a single character of the alphabet which serves as the predecessor and χ is the word (or string) called the successor. Note that if there are multiple rules with identical predecessors and differing successors, a probability may be assigned to each rule to determine the frequency at which each are utilized. As an illustrative example, we consider the following two production rules:

$$\begin{aligned} A &\rightarrow B[-A]x[+A]B \\ B &\rightarrow A \end{aligned}$$

To this point, the example is nearly a simple D0L-system (deterministic because the predecessors are non-repeating and context free) which is not specific to a map generation. The example put forth, however, may be applied to a mapping problem with the addition of a few rules.

In a mapping scenario, each letter of the axiom represents an edge of the initial map. Therefore the length of the axiom must be equal to the number of edges in the initial structure. It is also customary to include the special characters [,], +, and - when using a map L-system. When included in the production rules, the matching brackets, [and], indicate the inclusion of a marker which is labeled by the enclosed character. The orientation (+ or -) preceding the label in the closed brackets indicates the directionality of the marker, in this case the + symbol correlates to a counterclockwise placement of the edge. The remaining characters of the successor, which are not enclosed by brackets, indicate the number of segments the preceding edge is divided into. The new edges will be labeled as prescribed by the rules and nodes are placed between the edges. For example the first edge, A, which is the lower boundary of the map in figure 2, is discretized into three equal segments. The new edge segments are labeled, B, x, and B respectively. Between the first and second segments a marker oriented downward is placed and an upward oriented marker is placed between the second and third segments. Since the first marker is oriented outward from the map it is discarded while the second marker is eventually paired with the other inward facing marker on the upper boundary.

After all the pertaining edges are subdivided and markers are placed, the markers are checked for any possible pairings. As mentioned earlier, a pair of markers are matched if they belong to the same cell (are on the boundary of the same region), are not located on the same edge, if their labels are the same, and if they are oriented toward each other. There may be more than one potential set of marker pairs in a given cell, but the first pair to be found determines the location of the cell division. After cells are scanned for matching markers and the locations of the cellular divisions are determined, the remaining markers are discarded. The resulting maps generated in this example, for an initial square map with equal subdivisions of the edges, are shown in figure 2.

For the purpose of generating and optimizing topological maps in engineering applications it is useful to enforce a few additional constraints. After satisfying the previous conditions to create a cell wall, an eligible marker pair and its respective new edge must also meet certain limits prescribed by the user:

1. Prevention of small angles: the angles between the adjacent edges in the divided cells must be larger than a prescribed lower limit; this prevents the creation of cells with narrow angles.

2. Prevention of small areas: each newly formed cell must have a regional area which is greater than a prescribed percentage of the original map to avoid the formation of excessively small regions.

For practical problems, the structure must also have a finite number of edges. In some cases the cell divisions will cease when all edges of the map are labeled with a terminal token such (such as x in the previous example). Otherwise there exists a maximum number of iterations to be completed. Since this value is highly variable and dependent on the problem at hand, a number of iterations may be prescribed at the start of the map generation program or optimized in the genetic algorithm.

This section has provided a brief introduction to L-systems and an overview of the map L-system as is pertinent to topological map generations. For more details and information on Lindenmayer systems, the reader is referred to Prusinkiewicz and Lindenmayer [2004] and

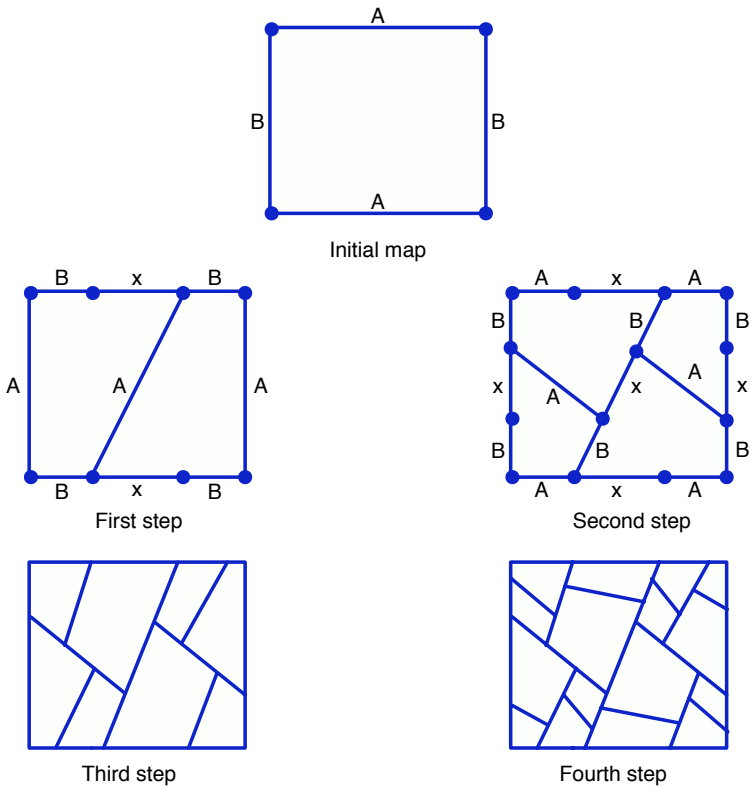

Figure 2: Example of the mBPMOL-systems process for the first four iterations where $\Omega = ABABA$and P: $A \rightarrow B[-A]x[+A]B$ and $B \rightarrow A$.

the references there in. The next section will further investigate the biological aspects of cellular division and their associated regulation mechanisms.

3 Fractones

In cellular biology the mitotic phase, or period of active cellular division, is generally a minor component of the overall cell cycle. A majority of the cell's time is rather spent in preparation for a cellular division, where accumulation of mass and nutrients and synthesis of DNA occurs. Cell cycles may also be dormant at times when inactive time gaps are included Becker [2009]. While rapid cellular division may take place in the early stages of life to promote growth of the individual, the main purpose of cellular divisions in adult organisms is for the maintenance of the body. Adult cellular divisions are reduced to the replacement of damaged and aged cells and to meet the overall functional needs of the individual. As a result, the frequency of cellular divisions is highly variable and dependent on the type of cell and the physical state of the body. To accommodate these variable rates of demand, the cells will typically enter periods of arrest or dormancy until an external indicator is presented and initiates the division process.

For this engineering application, our interest lies in the regulation of the cell cycle. Many cells do not replicate very frequently and often branch from the cell cycle into a dormant phase until signaled to resume active division. In these cases the cell only begins to actively divide when initiated by an external source, most often by cell-type specific molecules known as growth factors. Our focus is in better understanding these control and regulation processes

which govern the cell cycle and initiate cellular divisions. Recent findings in the area of neurosciences have introduced new concepts for better understanding such regulatory processes. The results of these studies, which will be reviewed in this section, are the inspiration for the model presented in this work.

In adult neurogenesis, neurons are generated from neural stem and progenitor cells (NSPC). NSPC are localized in specific area of the brain, most notably the subependymal layer of the left ventricle Kerever et al. [2007] Mercier et al. [2003]. Neural stem cell differentiation and proliferation in these areas are also known to be governed by the presence of growth factors, but the details of this regulatory process have remained unknown.

It has been hypothesized that the extracellular matrix in the adjacent regions of the left ventricle wall also plays a contributing role in the initiation of cellular divisions. Close examination of these regions have brought attention to branched structures in the extracellular matrix which come in direct contact with the NSPC. This branched (stem and bulb) structure which binds to the NSPC has assumed the term, fractonesKerever et al. [2007] Mercier et al. [2003]. Fractones are believed to be associated with the material of basement membranes which is the surface tissue containing high concentrations of extracellular molecules (ECM). These extracellular molecules include heparan sulfate proteoglycans (HSPG) which is a known binding cofactor of growth factorsKerever et al. [2007].

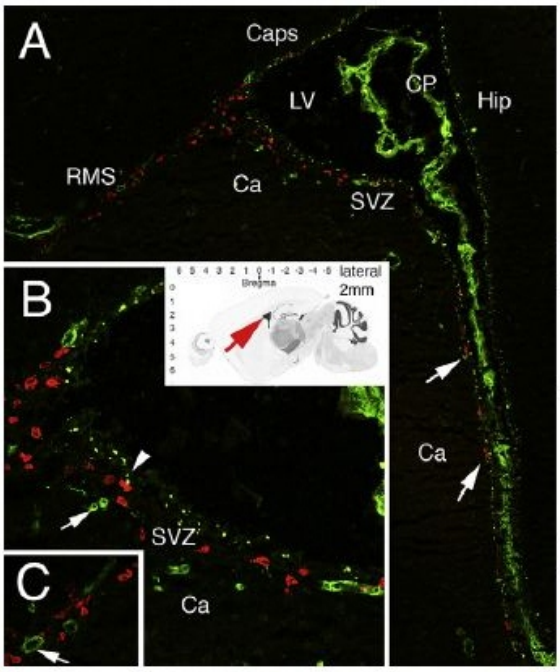

Figure 3: Cell proliferation and Fractones in the lateral ventricle: Fractones (arrows, green labeled N-sulfated HS) and proliferating cells (red labeled BrdU+) near the N-sulfated heparan sulfate fractone structures.

Imaging and statistical analysis methods have produced many new findings and evidence supporting the relationships theorized above. Molecules comprising the basement membranes have been identified in fractones structures, confirming that the two materials are indeed affiliated. A high density of cell proliferation was also observed near fractones, especially those containing N-sulfate HSPGKerever et al. [2007]. Immunolabeling techniques were performed to identify cells recently entering mitosis in several dissection samples. It was found that the majority of cells initiating cellular division were in the areas adjacent to fractones and capillaries, however statistical analysis revealed that cells initiating mitosis were generally in closer proximity to fractonesKerever et al. [2007]. These results indicate that fractones store the fibroblast growth factor 2 (FGF-2) via binding with HSPG and they are the main structures in relaying FGF-2 (growth factors) to the neural stem cells which then undergo mitosis.

The introduction to fractones presented here express the basic concepts that are of interest in this work. For further details on the analysis of fractones refer to Kerever et al. [2007] and Mercier et al. [2003].

4 The Fractone Map L-system

Thus far the map L-system and fractones have been introduced individually. In this next segment, the map L-system will undergo modifications to incorporate the idea of fractones and generate the resulting fractone map L-system.

It was previously demonstrated that fractones play a vital role in initiating division of their associated cells through the capture and delivery of growth factors from the extracellular space to the eligible cell. The model proposed here utilizes a similar and slightly simplified concept. For the purposes of this study, fractones are modeled as small and stationary structures which passively capture and consume simply diffusing growth factors. The fractones initiate mitosis in its neighboring cell once a threshold quantity of the growth factors is accumulated. The rates of growth factor accumulation in these structures are governed by a constant diffusion coefficient and the initial distribution of the growth factor molecules.

Integration of the fractones into the map L-system is accomplished by the assumption that all of the previously introduced markers in the map L-system represent fractones. All boundary and internal nodes also indicate active fractones (corner nodes are neglected). For simplification it is assumed that all markers (i.e. fractones) are actively consuming growth factors and remain active for the remaining iterations of the map generation. The fractones also have the same affinity for growth factors, and all fractones have the same threshold value. There is only one type of growth factor present in this model and the diffusivity of the molecule is constant throughout the system.

The diffusion of the growth factors along the edges is approximated with a one dimensional, piecewise linear finite element scheme. Diffusion is modeled along each line segment between markers and each segment is discretized with a constant number of uniform nodes. The source term of the diffusion equation is set to zero and the initial distribution of the growth factor is prescribed. All segment ends (fractone locations) are prescribed Dirichlet boundary conditions with a fixed concentration of zero.

The diffusion model is also prescribed a finite number of uniform time steps and after each time step, the amount of growth factors consumed at each node is computed. All eligible markers must accumulate the threshold value of growth factors in addition to satisfying all other requirements to form a pair and initiate a new cell wall formation. One example for such a case where the fractones influence the topology can be seen in figure 4.

After each iteration of the map generation when additional markers are placed and new walls may be formed, the growth factors are redistributed. For each existing segment that undergoes new subdivisions, the total quantity of growth factor is conserved and distributed among the new subsections. The existing growth factors of the edge are accumulated and dispersed with a weighted distribution governed by the length of each new segment. When a new wall is formed, an initial concentration of growth factors must also be assigned. In this case the average growth factor concentration of all existing segments is computed and assigned to the newly formed wall segments. This averaging is performed to remove any bias of wall formations at this member due to extremely low or high concentrations of growth factors relative to the remaining edges.

The growth factor concentrations for these calculations are carried over from the previous iteration in the map generation. If a pair of markers were matched in the preceding iteration, the growth factor concentrations of all edges during the first time step in which both markers reached the threshold value, serve as the initial conditions for the next iteration of the map. If there were no matching pairs in the previous iteration, the growth factor concentrations along all the edges during the last time step are the values carried over to the next iteration of the map generation.

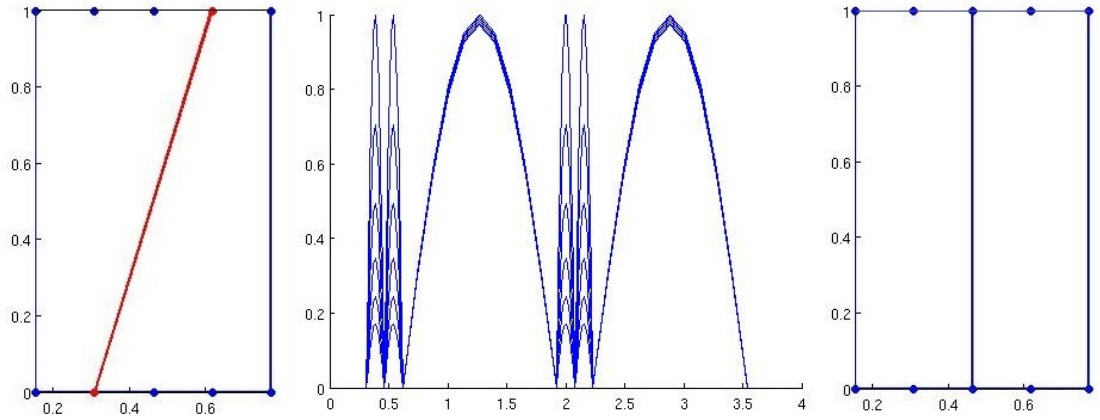

(a) (b) (c)

Figure 4: First iteration of a mapping with and without fractones with axiom: ABAB and production rules:A $\rightarrow$ B[+A]x[+A]x[+A]B and B$\rightarrow$A: a) First subdivision using original mapping system b) Diffusion of growth factors along linearized edges of the map (starting at bottom edge): GF concentration vs. x c) First subdivision using fractone mapping system

While this method is more complex and requires greater computational time to generate maps compared to the original map L-system, it has the potential to improve the overall performance of the optimization with the addition of the diffusion parameters in the genetic algorithm. This scheme may prove to be beneficial when applied to complex optimization problems such as the application presented in the next section.

5 Flapping Wing Optimization

An aeroelastic flapping membrane wing model Stanford et al. [2011] will serve as the test application of the above mentioned optimization methods. This problem analyzes the performance of a forward flight flapping membrane wing for a micro air vehicle. These bio-inspired wings are comprised of thin, flexible membranes reinforced with a rigid beam network, similar in form to the veined wings of insects. The performance of the wing structures are influenced by the venation patters of the supporting members and it is this topology which will undergo optimization. Both the original and fractone inspired map L-systems will be applied independently and the resulting maps will be used to generate the Pareto curves parameterized by the designs power requirement and thrust generation.

Evaluation of the wings under the given flight conditions are to be accomplished as follows. The structural modeling of the wing will be completed using a finite element analysis of the membranes with a triangular mesh (figure 5). The respective governing equation is applied to each element of the membrane:

$$N_x \cdot w_{,xx} + 2N_xy \cdot w_{,xy} + N_y \cdot w_{,yy} + f_z(x,y,t) = \rho \cdot w_{,tt} \tag{1}$$

where N is the pre-stressed resultants, w and f are the out-of-plane displacement and applied force per area, and ρ is the membrane density per length. The Euler-Bernoulli equation is used to analyze the beam members (battens, leading edge, tip, and root) Stanford et al. [2011].

The governing equations are converted into the usual finite element matrix form:

$$M \cdot u'' + C \cdot u' + K \cdot u = F \tag{2}$$

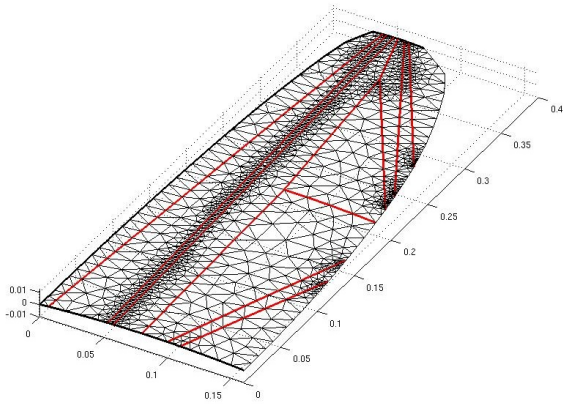

Figure 5: Finite element mesh of a sample wing design: triangular mesh of membrane, battens (red)

where M is the mass matrix, C is the damping matrix, K is the stiffness matrix, F is the accumulated load vector, and u is the total deformation of the structure Stanford et al. [2011] Eric B. Becker and Oden [1981]. Here the solution, u, is also approximated with a linear combination of modes:

$$u = \Phi \cdot \eta \tag{3}$$

where Φ is the modal matrix of natural vibrations and η is the modal amplitudes.

Prior to evaluating the performance of the wing designs, a few parameters must be defined. The flight kinematics are characterized by two angles of the wing, the first is the static angle of attack with respect to the external flow, α, and the second value, β, prescribes the range of the sinusoidal flapping. A constant velocity is also defined for the external air flow and a body attached coordinate system is utilized for the remaining computations.

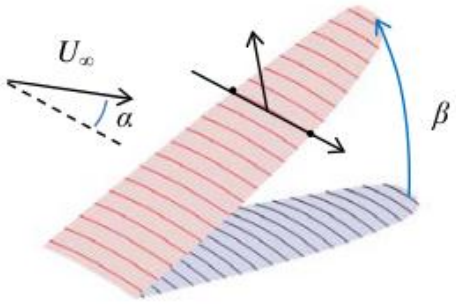

Figure 6: Characteristic angles and span-wise stations of the flapping wing with an attached coordinate system

The aerodynamic loads as opposed to the structural analysis are evaluated with a number of span-wise cross-sections of the wing. The pressure across the wing is determined by applying the no-penetration condition at each span-wise station:

$$\overline{\nu} + \lambda = u_o \cdot \frac{\partial h}{\partial x'} + \frac{\partial h}{\partial t} + \nu_o + \nu_1 \cdot x'/b \tag{4}$$

where h is the shape of the wing, u_o is the horizontal velocity, the last three terms are the vertical velocity (where b is the local semi-chord), and $\overline{\nu}$ and λ are the induced flow from the bound and trailing circulations Stanford et al. [2011]. The terms h, $\overline{\nu}$ and λ are transformed using the Glauert space $\varphi = acos(x'/b)$ for computations henceforth and the resulting integrations are computed using a defined set of Gaussian integration points.

The loads acting over each span section are computed using:

$$F_{y'} = \int_{-b}^{b} \Delta P \cdot dx' + F_{y'}^{\nu} \tag{5}$$

$$F_{x'} = \int_{-b}^{b} \Delta P \cdot \frac{\partial h}{\partial x'} \cdot dx' - 2\pi \cdot b \cdot \rho_{\infty} \cdot (nu_o + h_o - \lambda_o + u_o \cdot \Sigma n \cdot \frac{h_n}{b})^2 + F_{x'}^{\nu} \tag{6}$$

and the respective viscous terms are computed as follows ($F_{y'}^{v}$ is determined similarly):

$$F_{x'}^{v} = b \cdot \rho_i nfty \cdot U_{\infty}^2 \cdot (C_{D0} \cdot cos^2\alpha_s + C_{D\pi/2} \cdot sin^2\alpha_s) \cdot u_o/\sqrt{u_o^2 + v_o^2} \tag{7}$$

$$\alpha_s = atan(\frac{h(-b) - h(b)}{2b}) + atan(\frac{v_o}{u_o}) \tag{8}$$

where α_s is the local angle of attack, and C_{D0} and $C_D\pi/2$ are the drag coefficients at angles 0 and $\pi/2$ respectively.

A coupling of the two previous models (structural and airload) is employed to solve for the wing response at each temporal state. The loads are solved for at each cross-sectional segment and interpolated into the structural finite element mesh. The value of the pressure is evaluated at the center of each finite element and considered to be constant over the entire element. The deformation of the wing is determined and the wing shape is updated.

When the air vehicle is subjected to time-periodic flight conditions, the above solution may also be assumed to be time-periodic upon degradation of any transient terms. Each complete flapping cycle may therefore be discretized in time and the set of time-monolithic solutions are approximated using a finite element method.

Further details and information on evaluation of this model may be found in Stanford et al. [2011] and the references therein.

5.1 Genetic Algorithm

Once the topological maps have been generated by the previously discussed scheme, there is then the need for a system to evaluate, analyze and optimize the maps to produce useful results. Here the topologies are optimized using a genetic algorithm (GA). Just as biological evolution continues to progress by the process of natural selection, the nature of this method is to mimic the evolutionary process by preserving the most fit individuals. Genetic algorithms also allow for mutations and hybridization of individuals to produce offspring, however the advantage here is that computational process is greatly accelerated compared to the conventional evolution process.

The genetic algorithm generally begins with strings of numbers (equal in length) which are analogous to genomes of a common species. Each numerical string represents one individual and the number of strings represents the population size, which is constant through each generation. The genomes are representative of the structures which are to be optimized; in this case each genome may be translated into a topological map by the (fractone) map L-system. The individual genes or elements of the string are used to generate the axiom and production rules associated with the map L-system. The first set of numbers in the genome is translated into the axiom, generating a character label and directionality for each initial edge

of the map. The majority of the genes used occur in the second extraction from the genome. This set generates the production rules which again prescribe a number of character strings and associated orientations for the markers. In the case of the fractone map L-system, an additional three genes are placed at the tail of the genome. These last three genes contain the values for the threshold, diffusivity, and initial concentration of the growth factors in the fractone model. The only constraint placed on these values is that the threshold value must be less than the initial concentration.

Once the genomes are translated into their associated maps, they are evaluated by a function unique to the problem at hand and each member of the population is ranked based on their "fitness". The most fit individuals are retained to repopulate the next generation of individuals by a combination of random mutation and cross-over of two parent genomes. The probabilities of crossover and mutation shall be cautiously selected by the user to ensure that the desirable characteristics are retained while allowing enough variation to avoid convergence at local optima. Once the offspring are generated, they are also evaluated for fitness and pooled together with the parent genomes. The combined population is ranked and the best genomes are selected to begin the next iteration. The process is completed when a prescribed number of iterations are achieved.

While a single objective optimization problem would be a straightforward example for determining "fitness" in a genetic algorithm, it is often desired that a multiobjective optimization be performed. In this case there is a defined constraint:

$$g(x) \leq 0 \tag{9}$$

and a vector of objective functions to be minimized:

$$\{f_1(x), f_2(x), \cdots, f_n(x)\} \tag{10}$$

This problem is solved using a non-domination ranking system in which designs are preferred if they perform superior to other designs in one or more of the objective functions. Generally there is no single optimum design, and rather a Pareto front is formed. The points along the Pareto optimum are characterized such that one objective function cannot be improved without compensation in another target function. A niching scheme based on the proximity of points is also employed and promotes a greater spread of the Pareto front. The topological designs contained in or closest to the Pareto front are ranked higher and favored in the selection of parents for the next generation.

The previous section presented the methodologies for performing a topology optimization using a biologically inspired fractone model. In this section the results are presented for an optimization of the venation pattern for a flapping membrane wing of a micro air vehicle. Both the original map L-system topology generation and the fractone map L-system methods are employed and the resulting performances are compared. Some optimal wing designs and their performances are introduced here along with some analysis of the Pareto fronts generated during the optimizations.

6 Wing Design

The wing structure was composed of a thin latex membrane and a carbon fiber lattice structure. The membrane was characterized with an isotropic pre-stress condition and the carbon fiber beams were prescribed a rectangular cross-section. These details, along with the remaining material and geometric properties of the wing are presented in Table 1.

The wing shape was defined with a root chord of 0.16 meters, a wing length of 0.4 meters, and a tip chord of 0.04 meters. A parabolic camber was prescribed with a maximum value

property	membrane	battens	leading edge
elastic modulus, E	2 MPa	300 GPa	300 GPa
Poisson's ratio, ν	0.5	0.34	0.34
density, ρ	1200 kg/m^3	1600 kg/m^3	1600 kg/m^3
thickness	0.1 mm	0.8 mm	2 mm
width	-	3 mm	5 mm
pre-stress, N_x, N_y	10 N/m	-	-

Table 1: Material and geometric properties of the membrane wing

of 2% the local chord length. There was no twist of the original wing, the dihedral angle was zero, and the angle of attack (α) was set to 4 °.

The kinematics of flight were parameterized with a flapping frequency (ω) of 40 rad/s and a 30 ° amplitude of sinusoidal flapping (β). The flow velocity (U_∞) was 10 m/s and the density of air (ρ_∞) was 1.225 kg/m^3. The drag coefficients, C_{D0} and $C_{D\pi/2}$, were 0.05 and 2 respectively.

A number of parameters were also prescribed for the evaluation process which computed the fitness of each wing design. The structural analysis of the wings was performed with a finite element method using 20 modes. Airload analysis was performed with 20 span wise wing stations with 20 Gauss points and 6 inflow states. The flight dynamics were computed using a total of 100 timesteps per flapping cycle and 5 full cycles.

Three coefficients were defined for the multidisciplinary optimization of the wings. The lift generation, thrust generation, and power requirements were evaluated as follows:

$$\begin{aligned} C_L &= -F_x/(0.5 \cdot \rho_\infty \cdot U_\infty^2 \cdot S) \\ C_P &= P/(0.5 \cdot \rho_\infty \cdot U_\infty^3 \cdot S) \\ C_T &= -F_y/(0.5 \cdot \rho_\infty \cdot U_\infty^2 \cdot S) \end{aligned}$$

where F represents the respective forces, P is the accumulated power, and S is the area of the wing. For this optimization all coefficients were averaged over the flapping cycle and the lift coefficient was selected for the constraint function. The critical C_L value had a magnitude of 0.4892 (corresponding to a recorded average lift required for maximum thrust) and the constraint function was defined as:

$$g(x) = C_L - 0.4892 \tag{11}$$

The thrust and power coefficients were retained as the two objective functions (f_1(x), f_2(x)) to generate the Pareto fronts. A population size of 200 individuals and 200 generations were used in the genetic algorithm. The crossover probability of the genomes was 0.8 and the probability of mutation was 0.1.

The map L-system was constrained to a 20 letter alphabet and a maximum of 8 letters per production rule. A total of 4 iterations in the map generation were allowed. Growth factor diffusion was assessed in the fractone map L-system with a fixed number and length of timesteps. A total of 5 timesteps were used in each iteration of the map generation and each step was uniform with a length of 0.1.

A large variety of skeletal designs were generated from the optimization schemes parameterized here. A glimpse at the diverse pool of the resulting topologies can be seen in figure 7. Here the most optimal designs for the power and thrust objective functions are displayed. Each set of structures were randomly selected from a fractone and non-fractone based optimization. The drastic differences in the power and thrust optimums are apparent as well

as the similarities of results generated within each set. Both skeletal structures for optimal power coefficients contain very few members. The optimal design produced using the fractone system is especially sparse, while the design generated without fractones includes some reinforcement of the trailing edge. Similarly both designs for optimal thrust closely resemble each other with higher densities of the lattice structures and the majority of the members oriented span-wise.

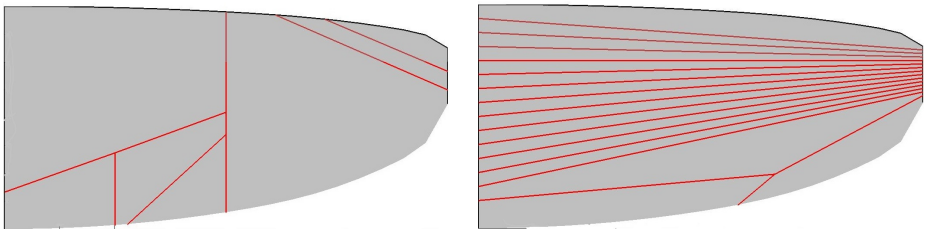

(a) Optimal power coefficient design without fractones: $C_{P,avg}$ = 0.3971, $C_{T,avg}$ = 0.1873, con_{avg} =0.0081

(b) Optimal thrust coefficient design without fractones: $C_{P,avg}$ =0.5270, $C_{T,avg}$ =0.2503, $con_{avg} = 4.79e^{-4}$

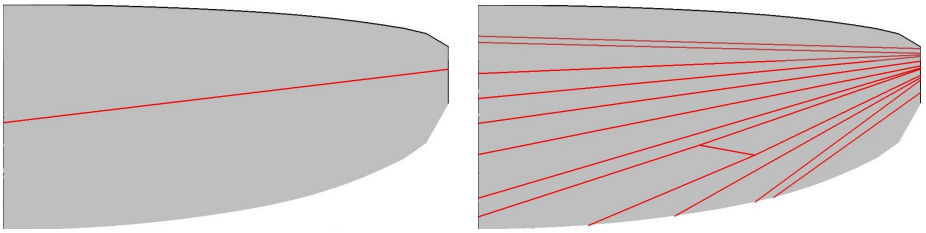

(c) Optimal power coefficient design using fractones: $C_{P,avg}$ =0.4085, $C_{T,avg}$ =0.1975, con_{avg} =0.0105

(d) Optimal thrust coefficient design using fractones: $C_{P,avg}$ =0.5142, $C_{T,avg}$ =0.2380, con_{avg} =0.0046

Figure 7: Optimal power and thrust coefficient designs

A selection of the resulting wings and their performances are presented in greater detail in figures 8 to 21. This collection includes a minimum power coefficient wing design resulting from the original map and fractone mapping systems in figures 8 and 15 respectively. An optimal thrust coefficient layout is also presented for the original and fractone mapping cases in figures 9 and 16 respectively. A total of five intermediate structures were also selected at random from each of the mapping scenarios and are displayed in figures 10 thru 14 and 17 through 21.

These results illustrate the structural dependence of the performances and correlate to the results found in Stanford et al. [2011]. As seen in the cases of the minimum power requirement designs, the lack of reinforcement at the trailing edge allowed for steeper gradients of displacement in the membranes. This allowed the wing a greater contour to the flow conditions and minimized the total power demand by reducing the aerodynamic resistance during both the upstroke and down-stroke of the flap. The compensation of this design however, was a reduction in peak thrust and lift performance. These designs (especially the fractone generated design with only one batten) had inferior lift performance to all other designs; while the lack of reinforcement allowed the wing to contour to more to flow, it reduced the occurrence of increased cambering and inflation.

In contrast to the power optimal designs, the stiffened thrust optimal designs exhibited reduced gradients with respect to the structures out-of-plane deformation. In both thrust optimal designs, the out-of-plane deformations were due to span-wise bending of the structures. During the down-stroke of these designs, when the lift was increased, it is seen that

the angle of attack was also slightly reduced and this favored the generation of thrust.

Interesting results are also observed in the inspection of the random designs. In many of these scenarios, inflation occurred where venation was sparse and large deformation gradients were formed. Presumably these occurrences favored a lift optimal design. An interesting design is also seen in figure 19, in which chord wise reinforcements were incorporated. This design resulted in intermediate performance in all three design variables between the thrust and power optimal designs.

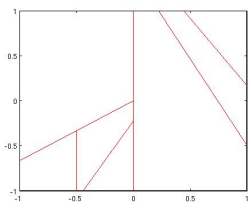

(a) Optimized map layout

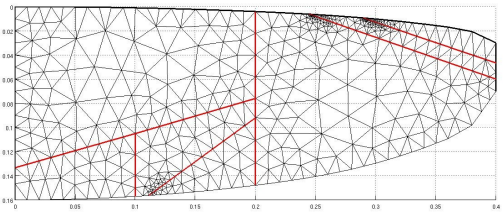

(b) Meshed wing structure

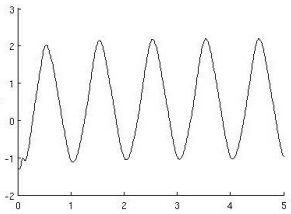

(c) Lift coeff vs. t/T , con_{avg} =0.0081

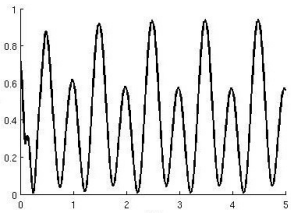

(d) Power coeff vs t/T, $C_{P,avg}$ =0.3971

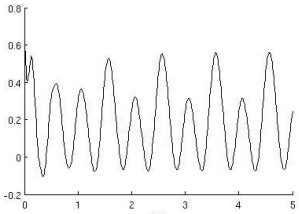

(e) Thrust coeff vs. t/T, $C_{T,avg}$ =0.1873

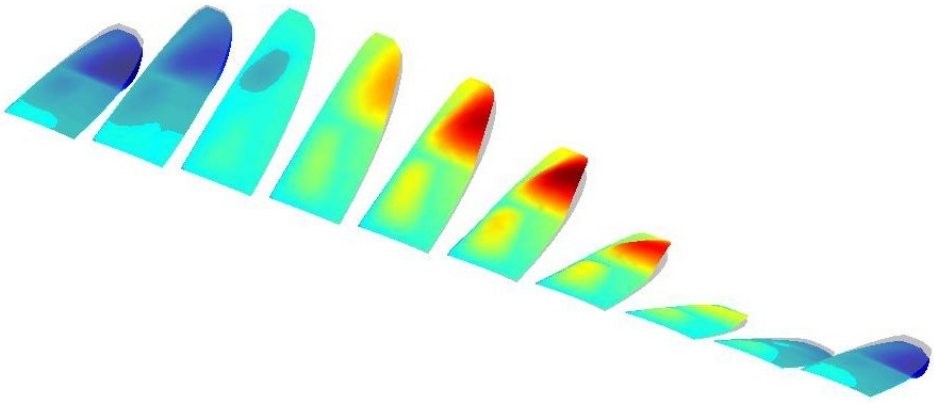

(f) Deformation of wing over a flapping cycle

Figure 8: Optimal power coefficient design: Original mapping system Run 1

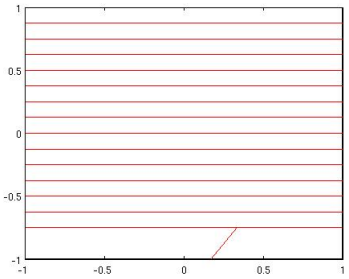

(a) Optimized map layout

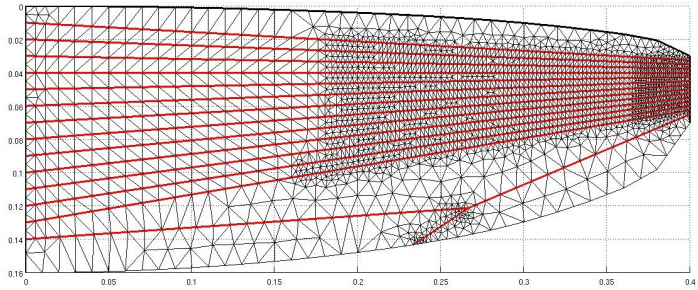

(b) Meshed wing structure

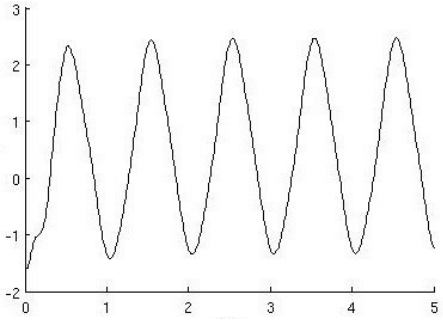

(c) Lift coeff vs. t/T , con_{avg} = $4.79e^{-4}$

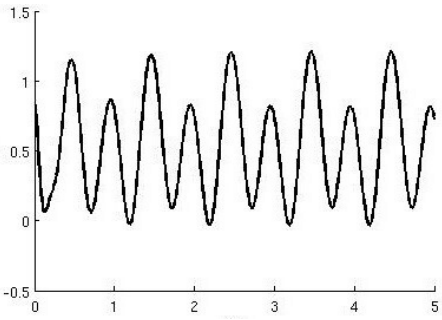

(d) Power coeff vs t/T, $C_{P,avg}$ =0.5370

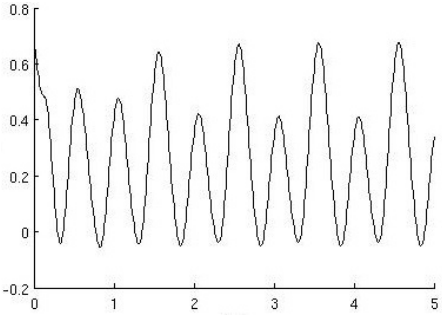

(e) Thrust coeff vs. t/T, $C_{T,avg}$ =0.2503

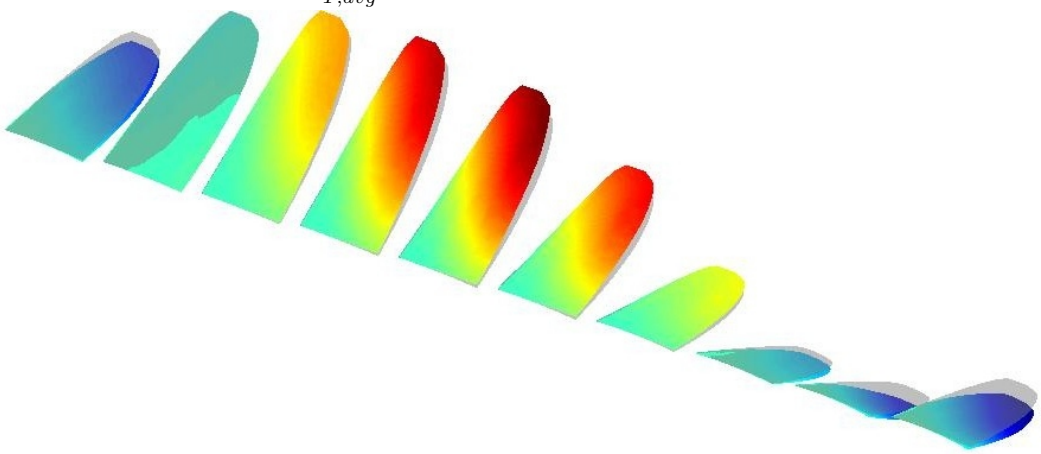

(f) Deformation of wing over a flapping cycle

Figure 9: Optimal thrust coefficient design: Original mapping system Run 1

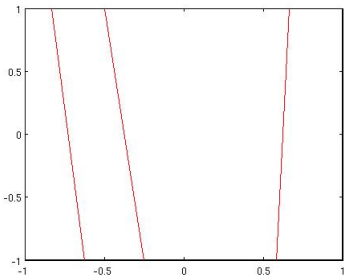

(a) Optimized map layout

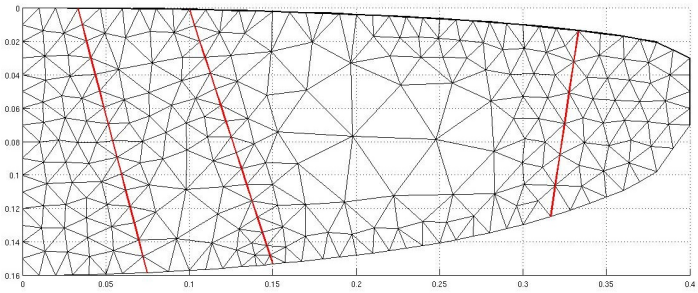

(b) Meshed wing structure

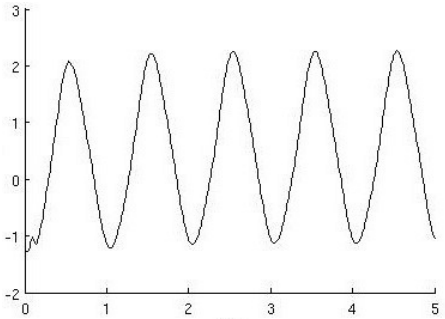

(c) Lift coeff vs. t/T , $con_{avg} = 0.0014$

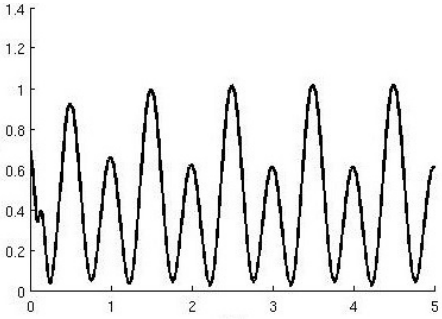

(d) Power coeff vs t/T, $C_{P,avg}$ =0.4325

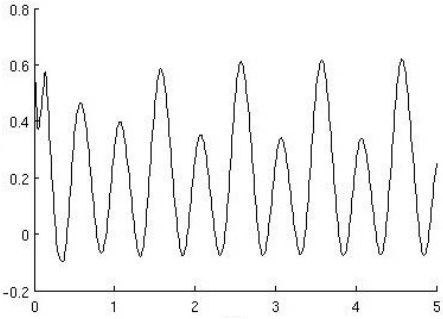

(e) Thrust coeff vs. t/T, $C_{T,avg}$ =0.2086

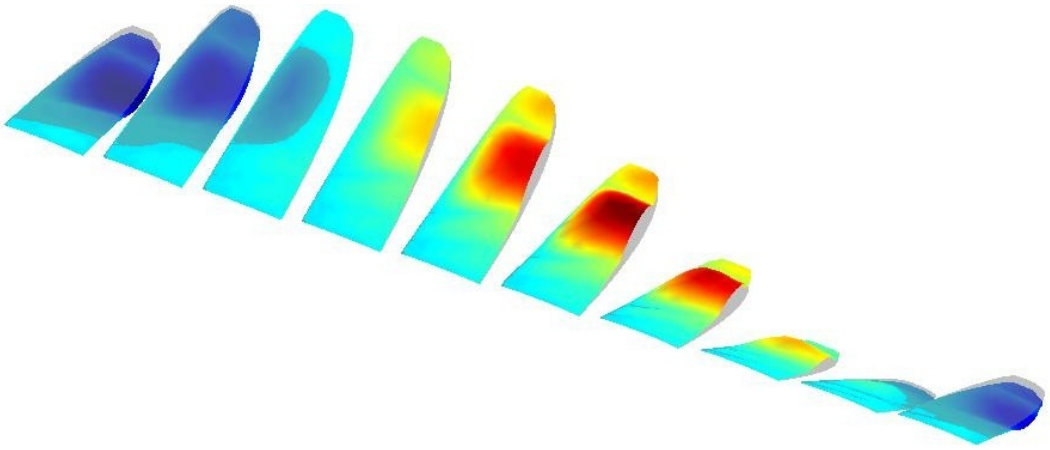

(f) Deformation of wing over a flapping cycle

Figure 10: Random design #1: Original mapping system Run 1

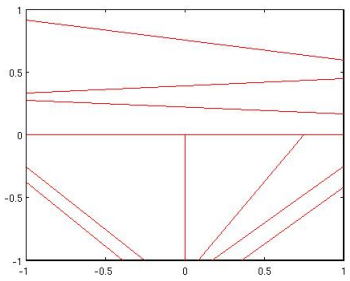

(a) Optimized map layout

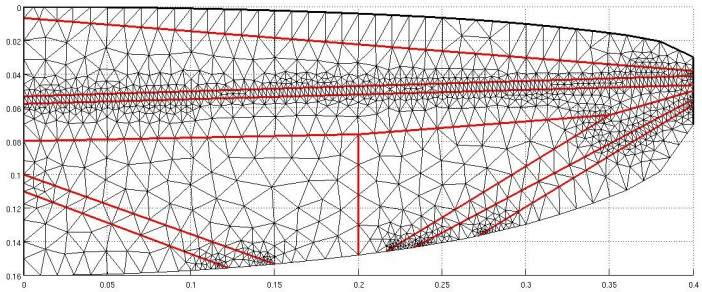

(b) Meshed wing structure

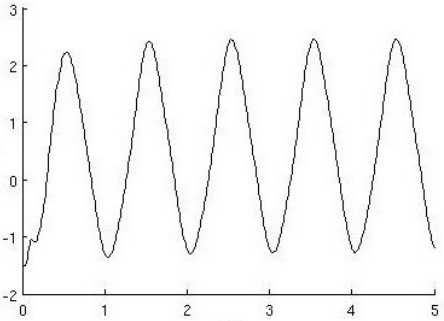

(c) Lift coeff vs. t/T , $con_{avg} = 0.0224$

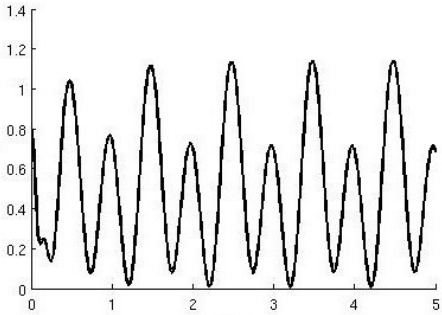

(d) Power coeff vs t/T, $C_{P,avg}$ =0.4936

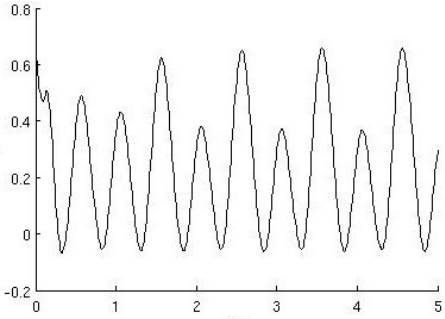

(e) Thrust coeff vs. t/T, $C_{T,avg}$ =0.2316

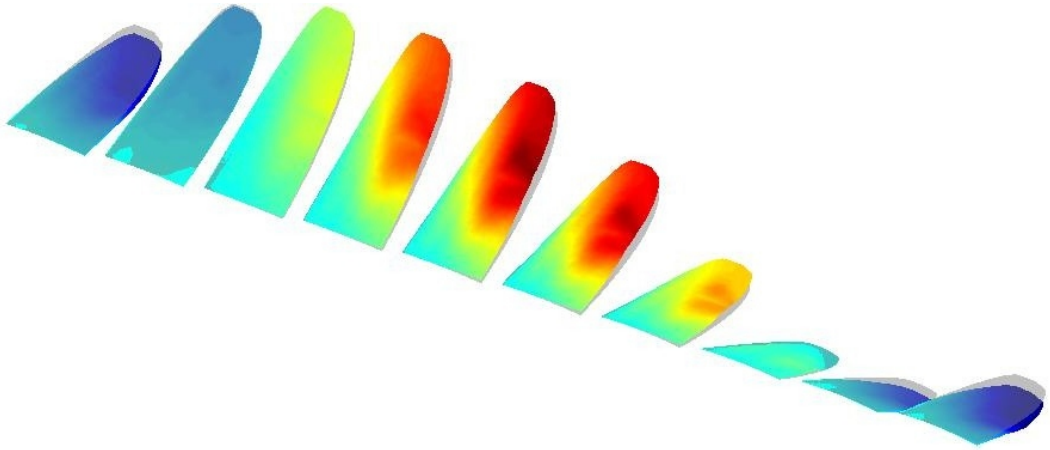

(f) Deformation of wing over a flapping cycle

Figure 11: Random design #2: Original mapping system Run 1

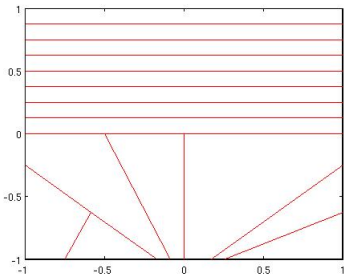

(a) Optimized map layout

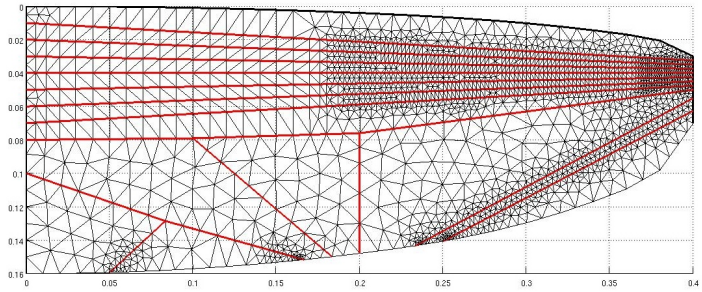

(b) Meshed wing structure

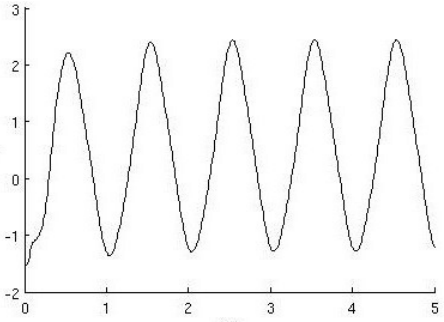

(c) Lift coeff vs. t/T , $con_{avg} = 0.0081$

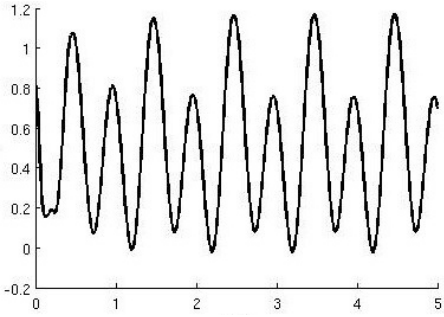

(d) Power coeff vs t/T, $C_{P,avg}$ =0.5039

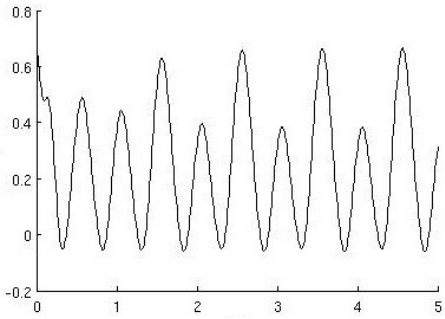

(e) Thrust coeff vs. t/T, $C_{T,avg}$ =0.2371

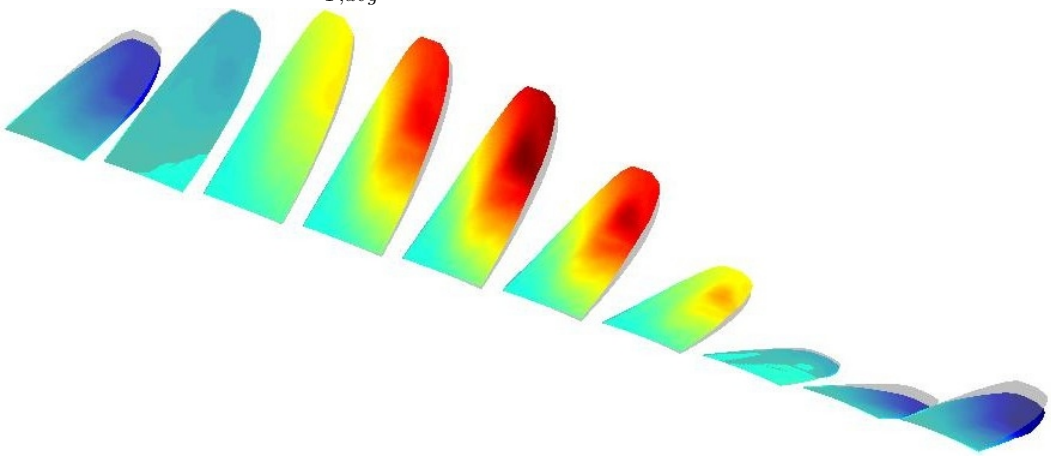

(f) Deformation of wing over a flapping cycle

Figure 12: Random design #3: Original mapping system Run 1

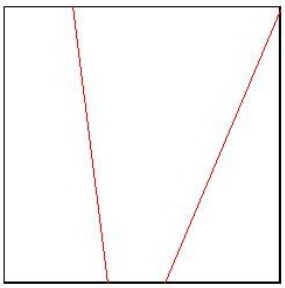

(a) Optimized map layout

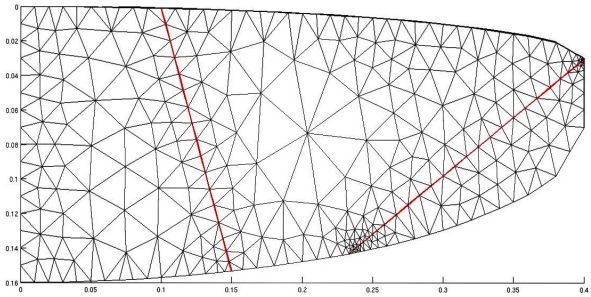

(b) Meshed wing structure

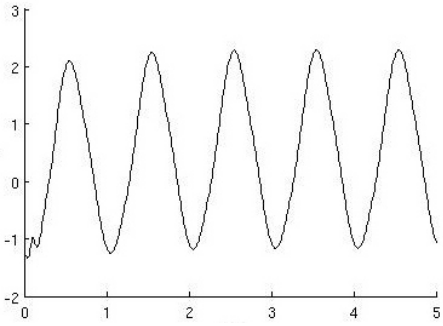

(c) Lift coeff vs. t/T , $con_{avg} = 0.0034$

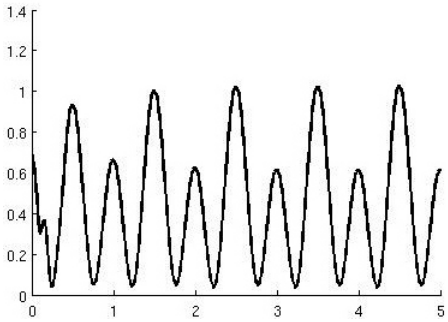

(d) Power coeff vs t/T, $C_{P,avg}$ =0.4390

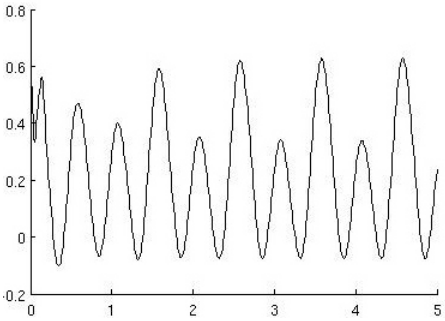

(e) Thrust coeff vs. t/T, $C_{T,avg}$ =0.2120

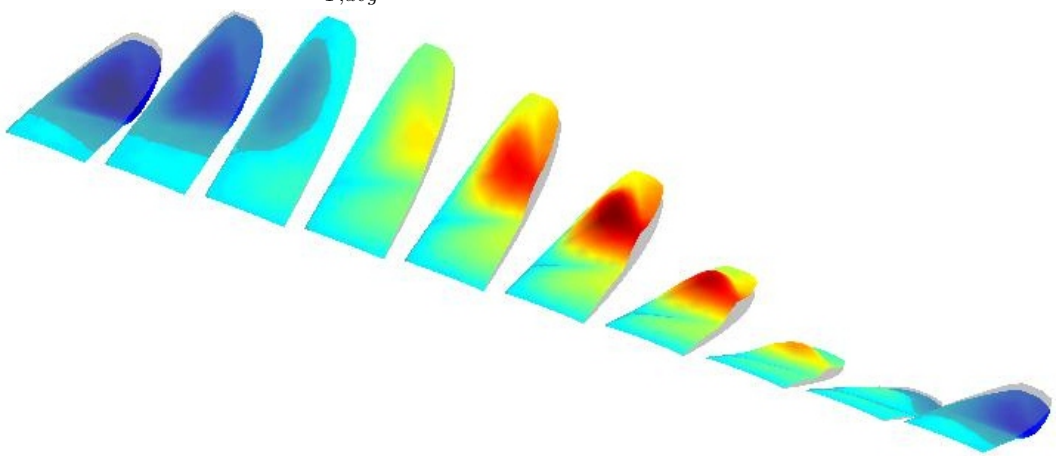

(f) Deformation of wing over a flapping cycle

Figure 13: Random design #4: Original mapping system Run 1

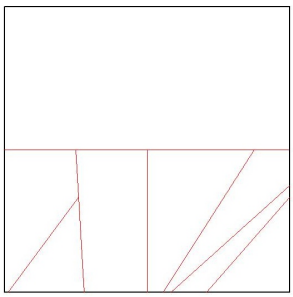

(a) Optimized map layout

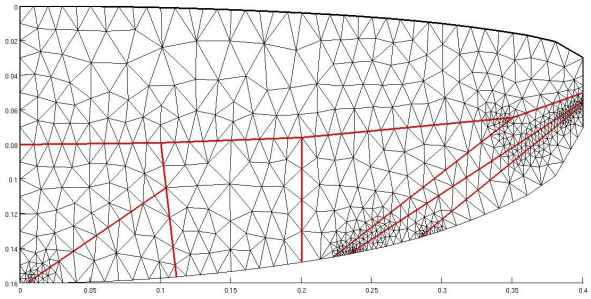

(b) Meshed wing structure

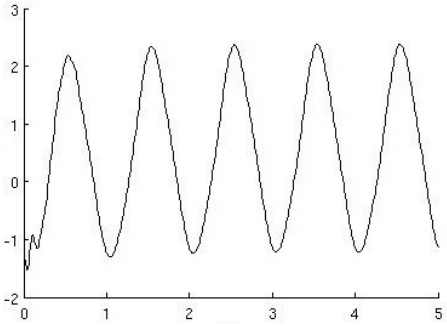

(c) Lift coeff vs. t/T , $con_{avg} = 0.0099$

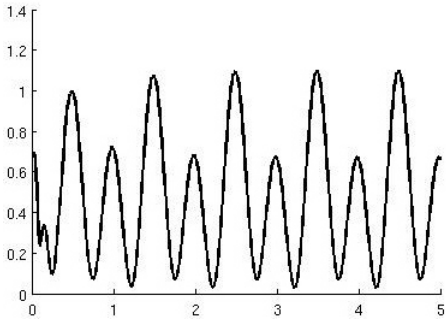

(d) Power coeff vs t/T, $C_{P,avg}$ =0.4750

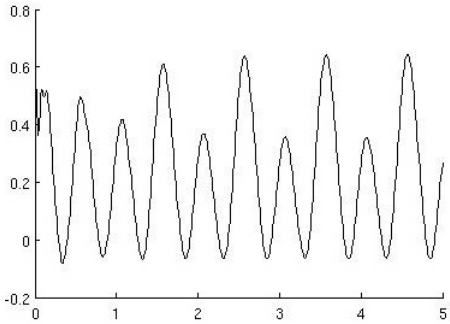

(e) Thrust coeff vs. t/T, $C_{T,avg}$ =0.2235

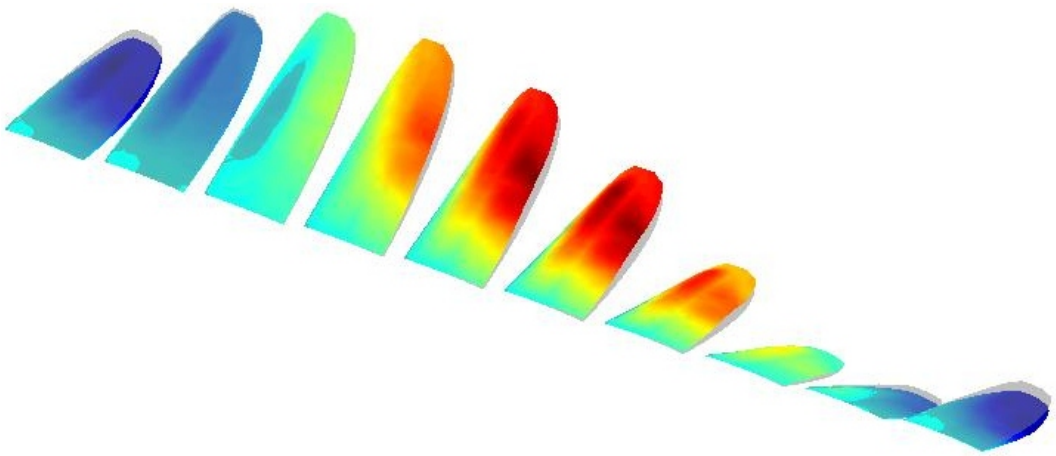

(f) Deformation of wing over a flapping cycle

Figure 14: Random design #5: Original mapping system Run 1

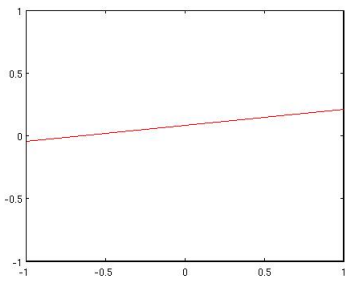

(a) Optimized map layout

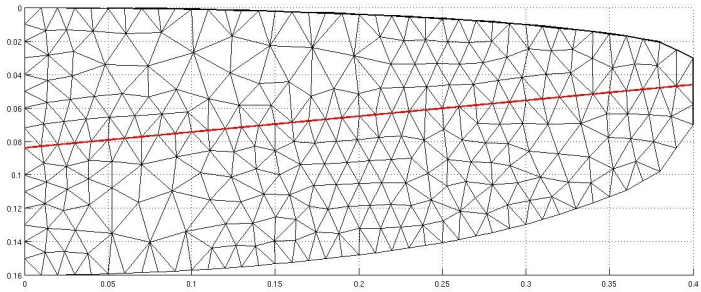

(b) Meshed wing structure

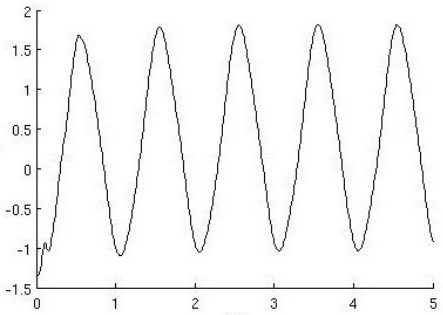

(c) Lift coeff vs. t/T , con_{avg} =0.0105

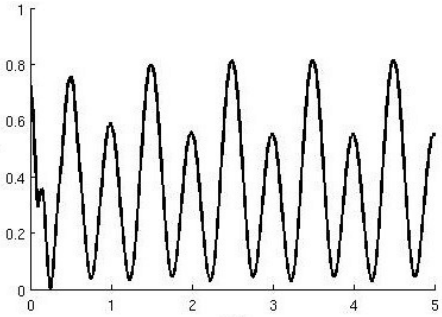

(d) Power coeff vs. t/T, $C_{P,avg}$ =0.4085

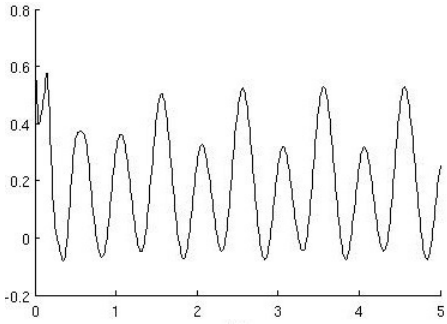

(e) Thrust coeff vs. t/T, $C_{T,avg}$ =0.1975

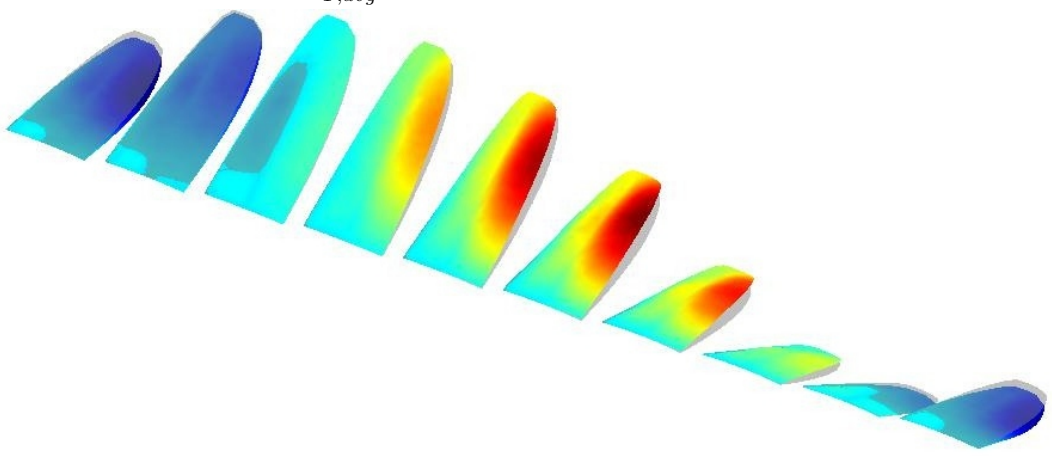

(f) Deformation of wing over a flapping cycle

Figure 15: Optimal power coefficient design: Fractone mapping system Run 2

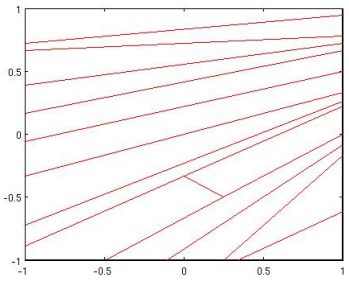

(a) Optimized map layout

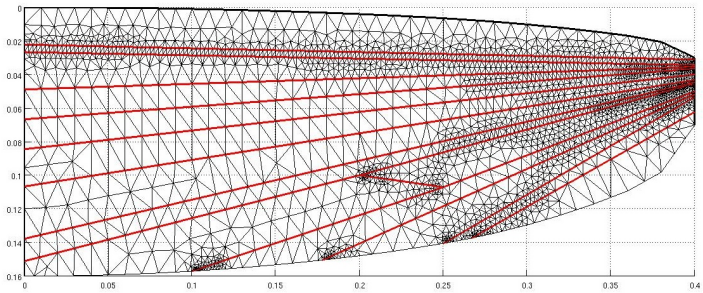

(b) Meshed wing structure

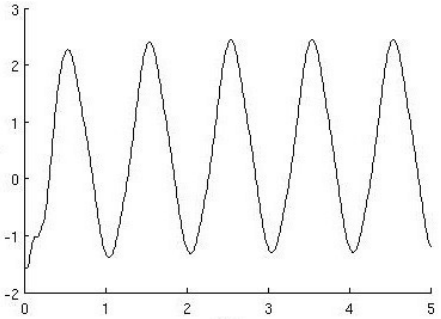

(c) Lift coeff vs. t/T , con_{avg} =0.0046

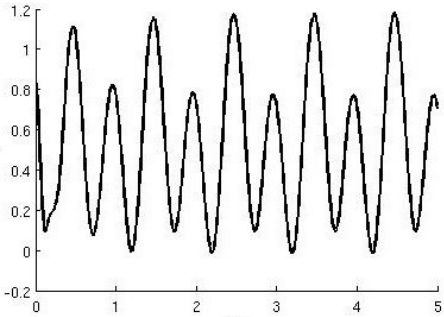

(d) Power coeff vs. t/T, $C_{P,avg}$ =0.5142

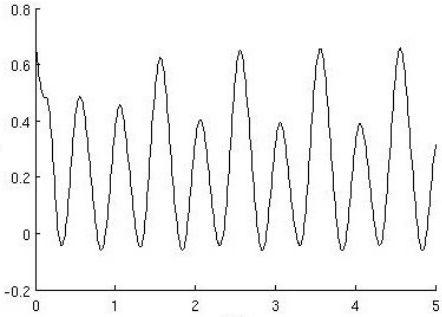

(e) Thrust coeff vs. t/T, $C_{T,avg}$ =0.2380

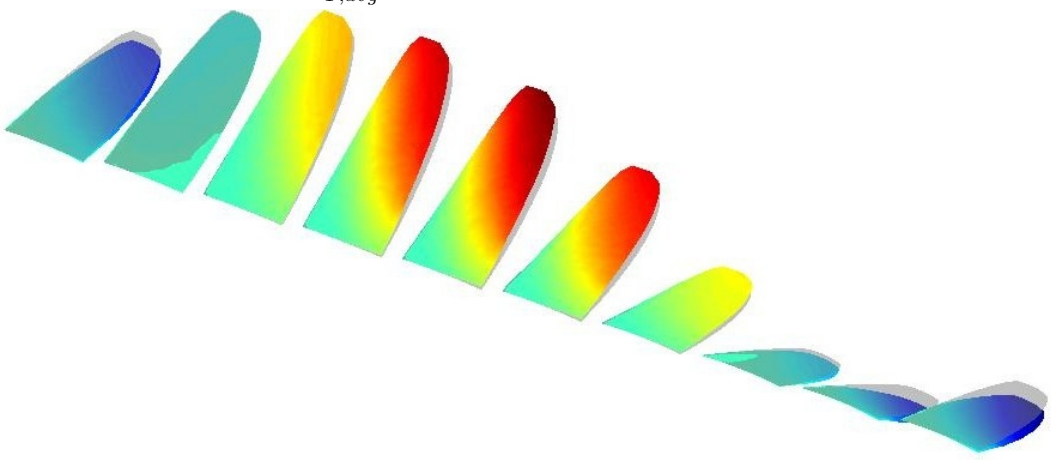

(f) Deformation of wing over a flapping cycle

Figure 16: Optimal thrust coefficient design: Fractone mapping system Run 2

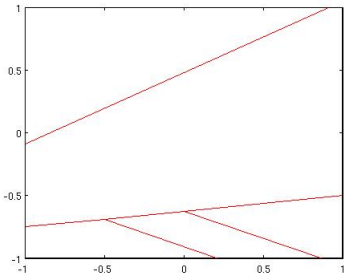

(a) Optimized map layout

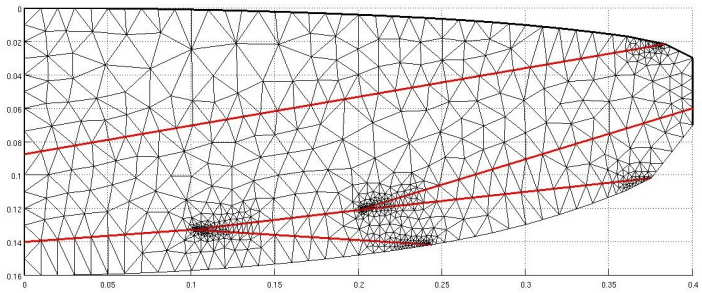

(b) Meshed wing structure

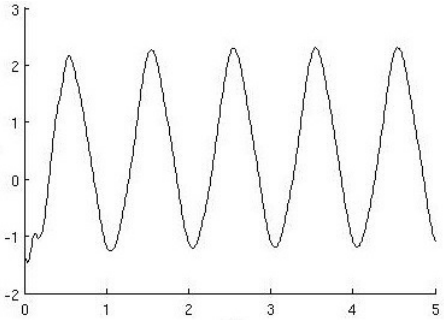

(c) Lift coeff vs. t/T , con_{avg} =0.0807

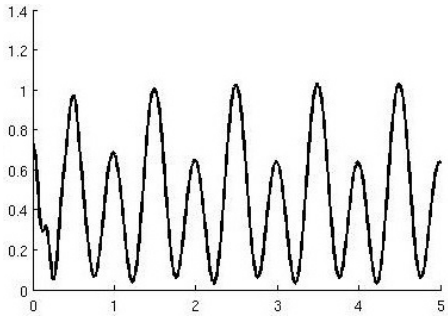

(d) Power coeff vs. t/T, $C_{P,avg}$ =0.4489

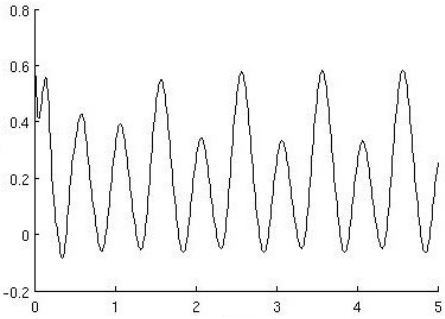

(e) Thrust coeff vs. t/T, $C_{T,avg}$ =0.2141

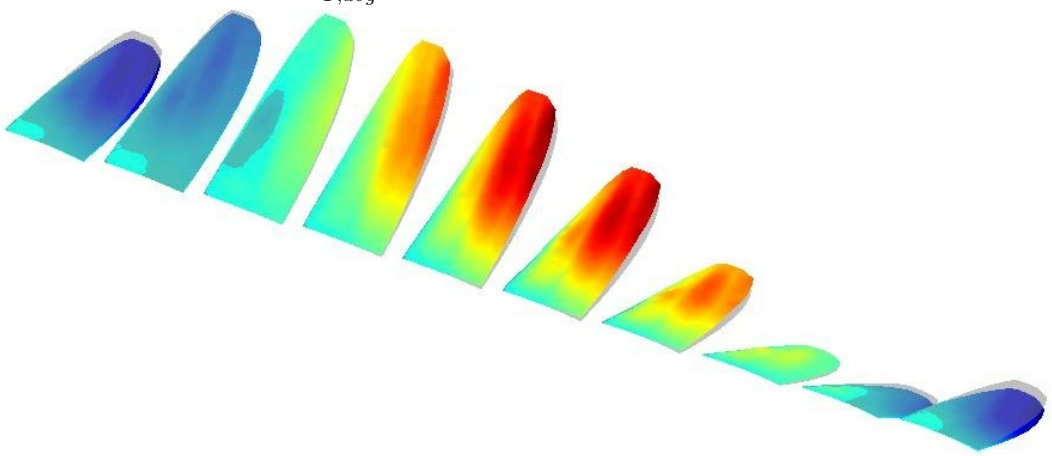

(f) Deformation of wing over a flapping cycle

Figure 17: Random Design #1: Fractone mapping system Run 2

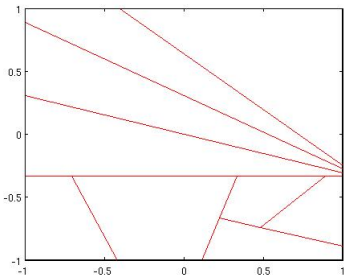

(a) Optimized map layout

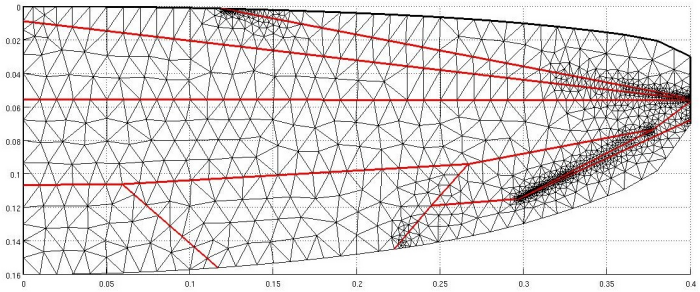

(b) Meshed wing structure

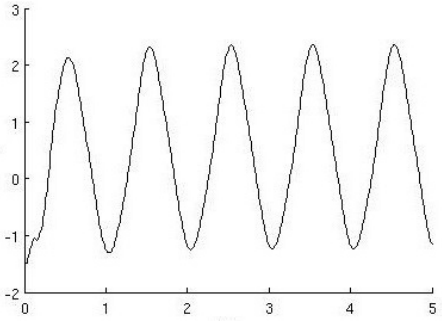

(c) Lift coeff vs. t/T , con_{avg} =0.0114

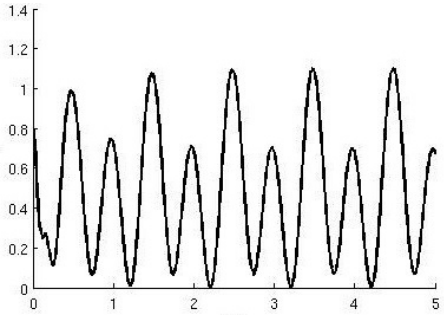

(d) Power coeff vs. t/T, $C_{P,avg}$ =0.4726

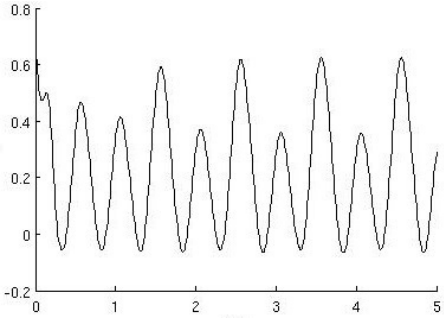

(e) Thrust coeff vs. t/T, $C_{T,avg}$ =0.2220

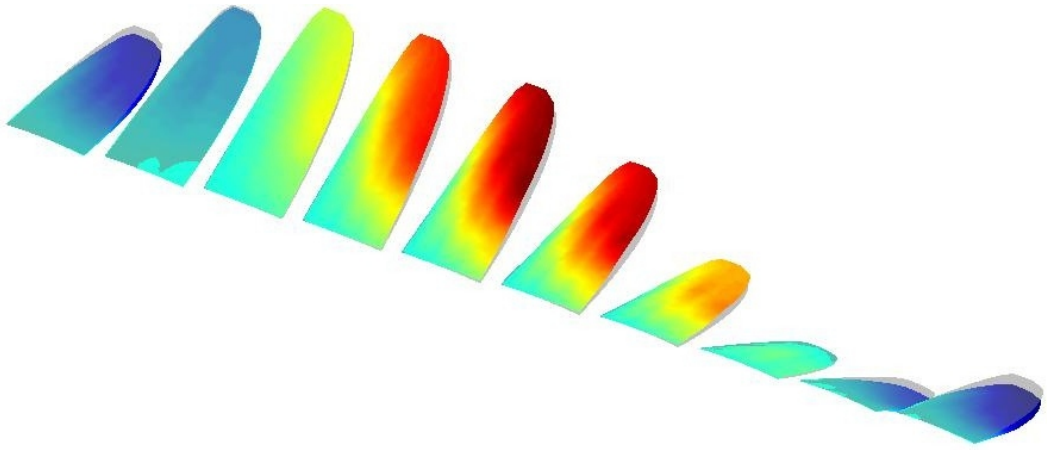

(f) Deformation of wing over a flapping cycle

Figure 18: Random Design #2: Fractone mapping system Run 2

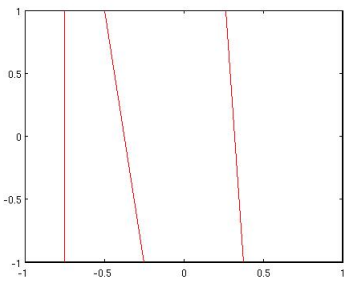

(a) Optimized map layout

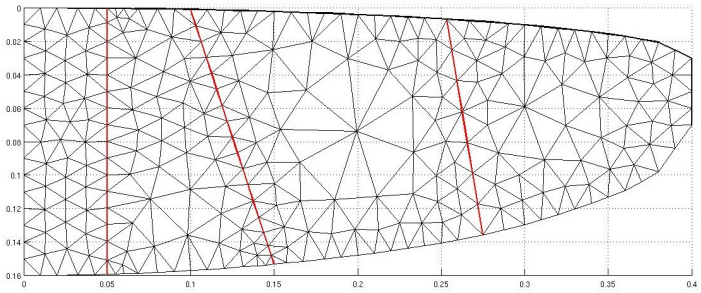

(b) Meshed wing structure

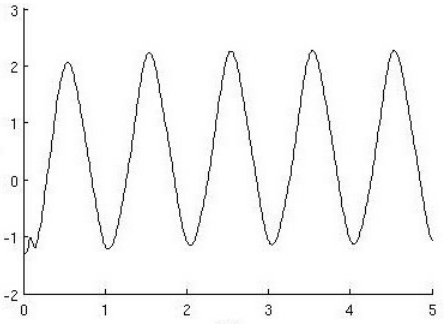

(c) Lift coeff vs. t/T , con_{avg} =0.0017

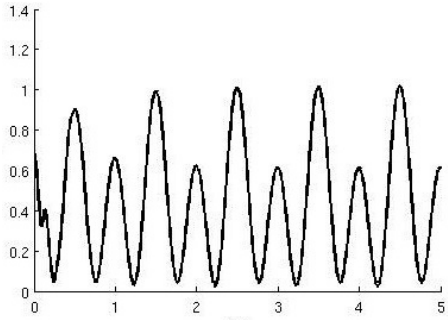

(d) Power coeff vs. t/T, $C_{P,avg}$ =0.4321

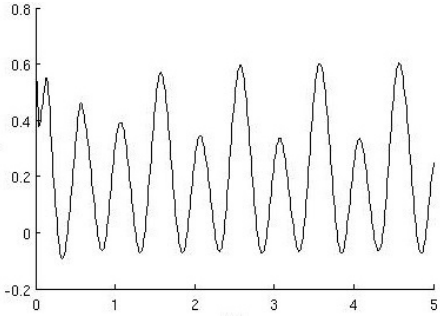

(e) Thrust coeff vs. t/T, $C_{T,avg}$ =0.2051

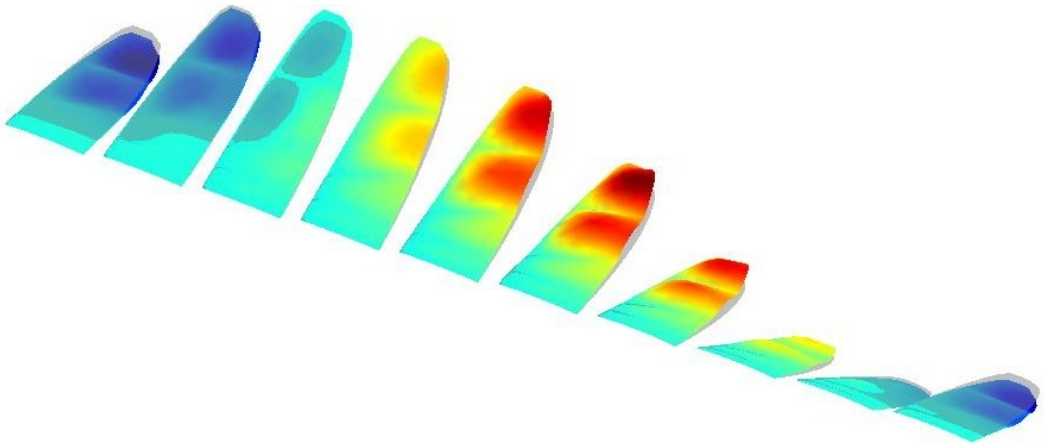

(f) Deformation of wing over a flapping cycle

Figure 19: Random Design #3: Fractone mapping system Run 2

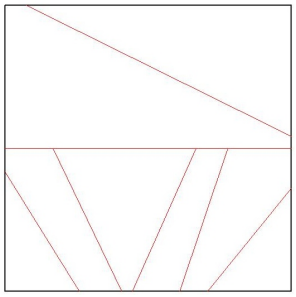

(a) Optimized map layout

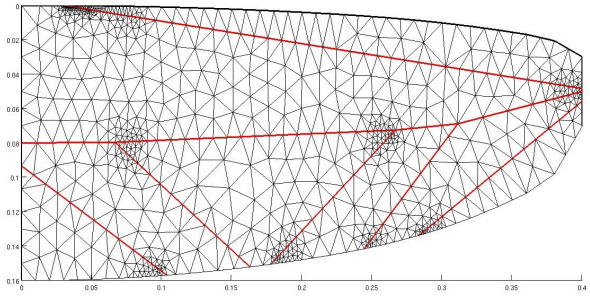

(b) Meshed wing structure

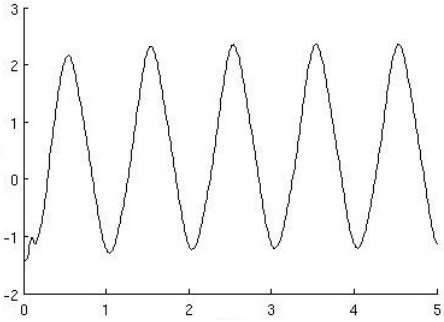

(c) Lift coeff vs. t/T , con_{avg} =0.0043

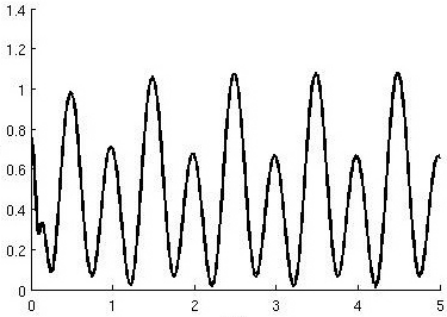

(d) Power coeff vs. t/T, $C_{P,avg}$ =0.4640

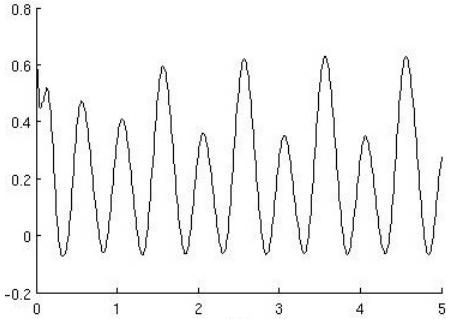

(e) Thrust coeff vs. t/T, $C_{T,avg}$ =0.2168

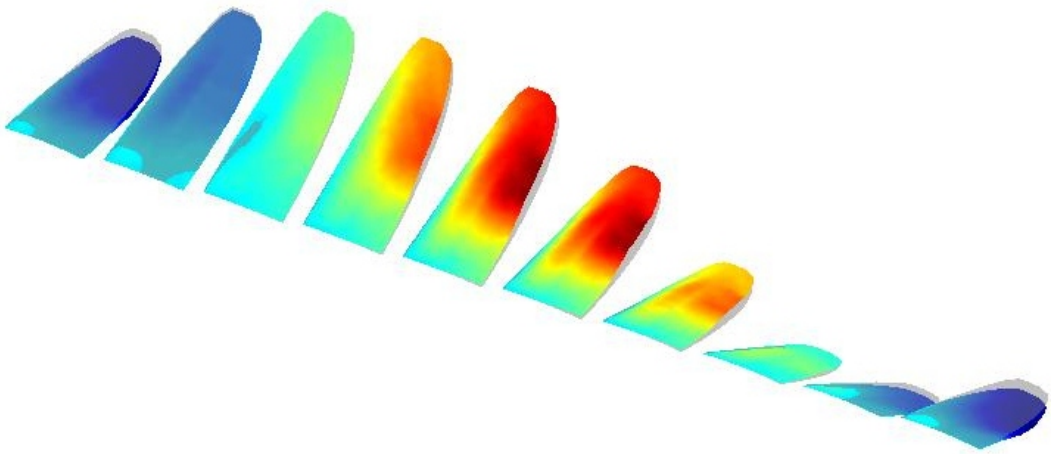

(f) Deformation of wing over a flapping cycle

Figure 20: Random Design #4: Fractone mapping system Run 2

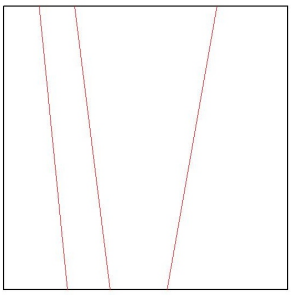

(a) Optimized map layout

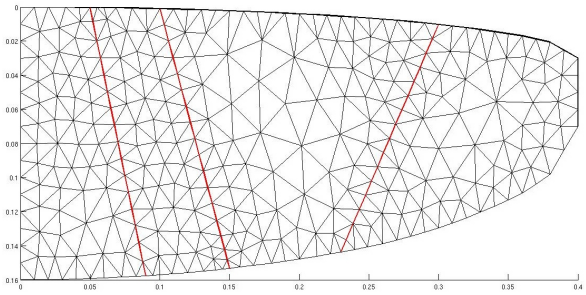

(b) Meshed wing structure

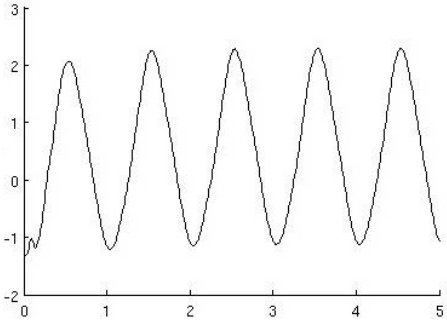

(c) Lift coeff vs. t/T , con_{avg} =0.0153

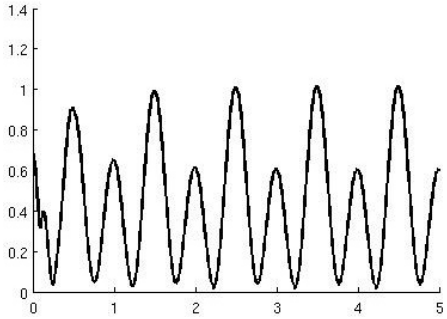

(d) Power coeff vs. t/T, $C_{P,avg}$ =0.4285

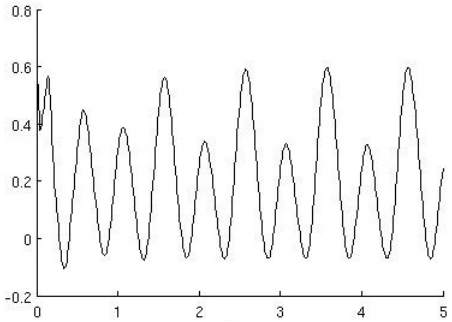

(e) Thrust coeff vs. t/T, $C_{T,avg}$ =0.2021

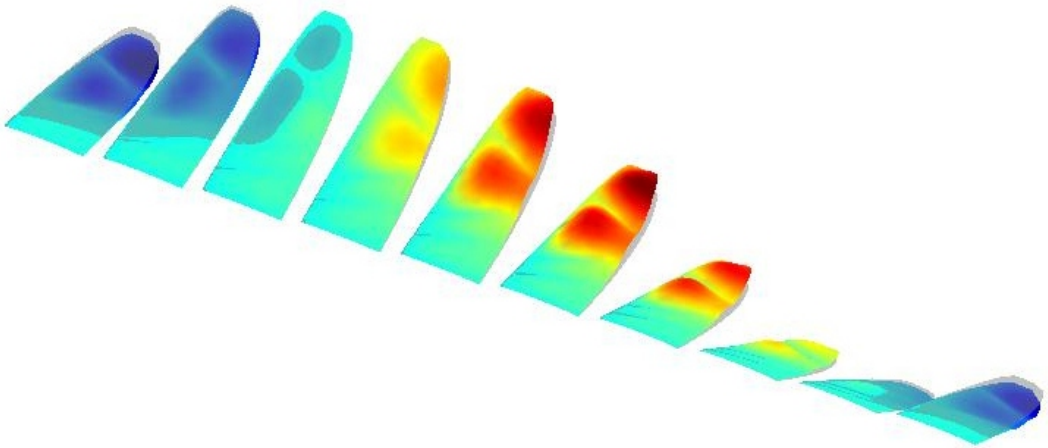

(f) Deformation of wing over a flapping cycle

Figure 21: Random Design #5: Fractone mapping system Run 2

7 Pareto Front Analysis

A total of ten trials were performed for each of the fractone and non-fractone optimizations. A typical Pareto front resulting in the final (200th) generation can be seen in figure 22. The Pareto front exhibited here illustrates a wide distribution of points as biased by the niching technique and superior performance of individuals compared to the other random designs.

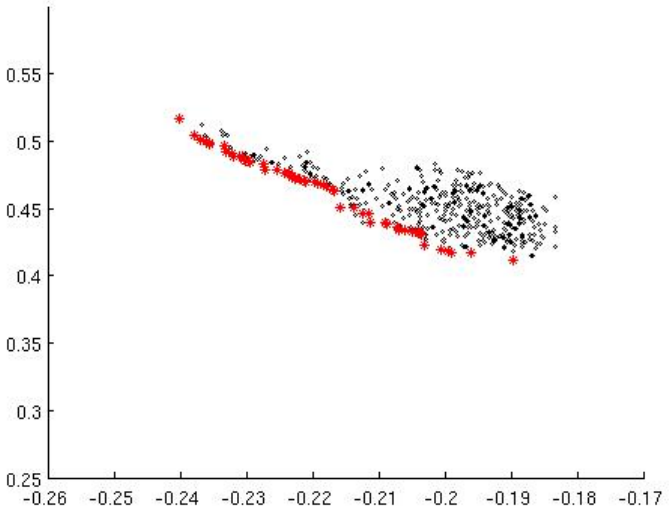

Figure 22: Sample Pareto Front (obtained from Run 2 without fractones):- Power coefficient vs. Thrust Coefficient, Pareto front (red) and other random designs (black)

7.1 Repeatability and Performance

The final Pareto fronts obtained from of each of the ten trials were collected to observe the repeatability of the algorithm. Figure 23 displays the repeatability of results from both the fractone and original mapping schemes. The two different methods appear to have comparable performances in terms of consistency as seen from the clustering of points and relatively narrow band-widths of the collected fronts.

The collection of Pareto fronts from the two methods were further combined in figure 24 to compare the fitness of the two methods. The dispersion of points belonging to the two cases are fairly even and consistent. While both methods seem to perform equally well on the thrust optimal end of the spectrum, the fractone mapping designs exceed the capabilities of the original mapping system for the majority of the spectrum as it progresses to the minimal power requirement designs. This is observed by the dominance of the fractone designs along the leading edge of the Pareto Front, especially along on the right hand side of the curve.

7.2 Convergence

To determine the convergence of the GA, the gradual nearing of the Pareto fronts were numerically approximated by computing an averaged norm. The distance from the highest ranked points in each iteration to the set of points in the final (200th generation) Pareto front were estimated and averaged for each approaching generation. The resulting convergence rates were compiled and averaged and can be seen in figure 25. Here the convergence rates

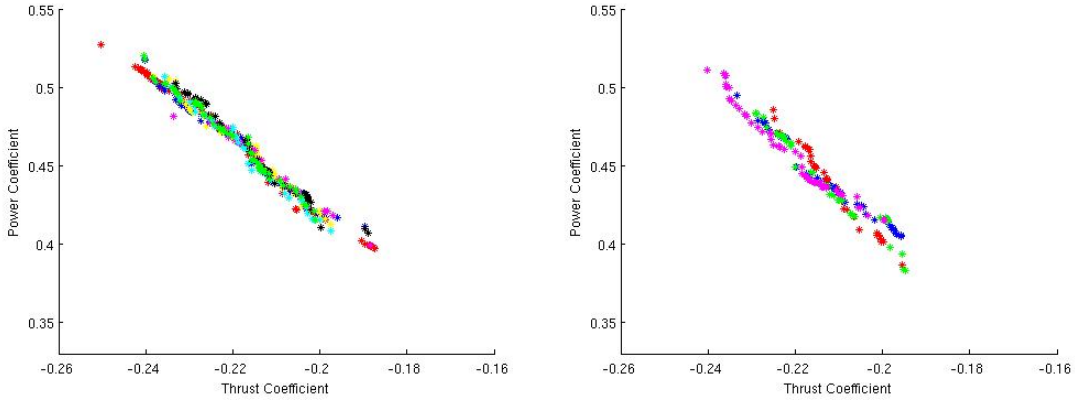

(a) Original mapping (no fractones) (b) Fractone mapping

Figure 23: Final Pareto fronts collected from runs 1 through10 (each test batch displayed in different colors and markers)

appear to be comparable, however, the rate of convergence with the fractone mapping scheme continuously improves over the 200 generations while the original methods quickly converges during the first few iterations and then levels off. The convergence of the fractone model is more consistent and it should be noted that the convergence rates are with respect to the final Pareto Fronts of each case and the final results of the fractone model were generally superior.

8 Conclusion

The results of these preliminary tests indicate that the performance of the fractone modified mapping system are in fact superior to the conventional mapping system used for topology optimization. Since the inclusion of fractones results in a competitive method for generating maps, new methods have the potential to further improve the performance and convergence of topology optimizations should the simple system be revised.

Future studies may test the effects of more complex fractone systems that incorporate multiple and competing growth factors, source terms, variations in the initial distributions, and removal or deactivation of fractones themselves. Inclusion of these additional control parameter could provide greater control of the final designs and improve the overall efficiency and capabilities of the process.

References

G. Allaire. *Shape Optimization be the Homogenization Method*. Springer, New York, 2002.

W. Becker. *The World of the Cell*. Pearson/Benjamin Cummings, 2009. ISBN 9780805393934. URL `http://books.google.com/books?id=dV-8PwAACAAJ`.

M. P. Bendsøe and O. Sigmund. *Topology Optimization: Theory, Methods and Applications*. Springer, New York, 2nd edition, 2003.

J. Deaton and R. Grandhi. A survey of structural and multidisciplinary continuum topology optimization: post 2000. *Structural and Multidisciplinary Optimization*, 49(1):1–38, 2014.

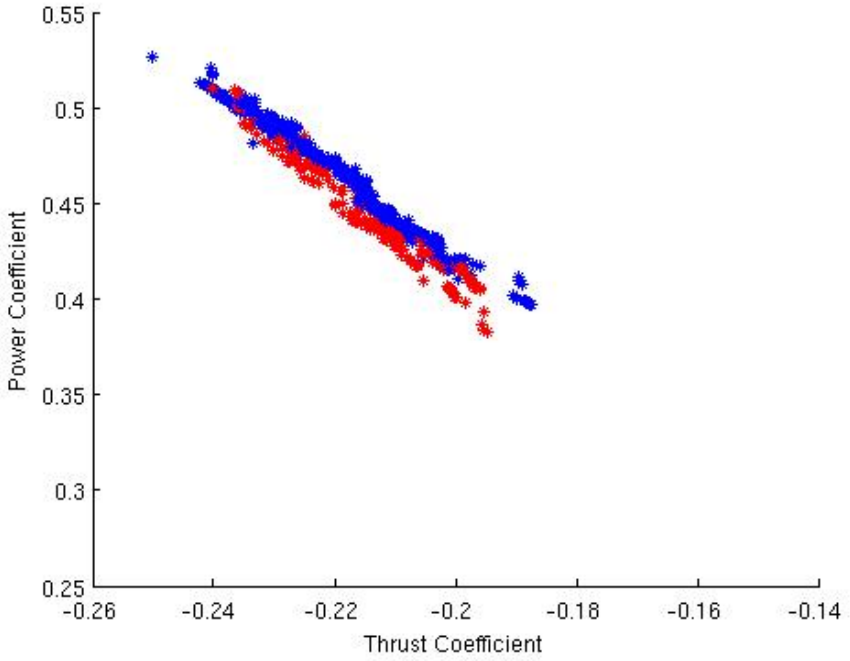

Figure 24: Collection of final Pareto fronts from 10 runs: fractone mapping in red, original mapping in blue

G. F. C. Eric B. Becker and J. T. Oden. *Finite Elements An Introduction : Volume I.* Prentice Hall, New Jersey, 1981.

A. L. Gain and G. H. Paulino. A critical comparative assessment of differential equation-driven methods for structural topology optimization. *Structural and Multidisciplinary Optimization*, 48:685–710, 2013. doi: 10.1007/s00158-013-0935-4.

A. Kerever, J. Schnack, D. Vellinga, N. Ichikawa, C. Moon, E. Arikawa-Hirasawa, J. T. Efird, and F. Mercier. Novel extracellular matrix structures in the neural stem cell niche capture the neurogenic factor fibroblast growth factor 2 from the extracellular milieu. *STEM CELLS*, 25(9):2146–2157, 2007. ISSN 1549-4918. doi: 10.1634/stemcells.2007-0082. URL `http://dx.doi.org/10.1634/stemcells.2007-0082`.

M. H. Kobayashi, H.-T. C. Pedro, R. Kolonay, and G. Reich. On a cellular division method for aircraft structural design. *The Aeronautical Journal of the Royal Aeronautical Society*, 113:821–831, 2009.

R. M. Kolonay and M. H. Kobayashi. Optimization of aircraft lifting surfaces using a cellular division method. *Journal of Aircraft*, 52(6):2051–2063, 2015.

F. Mercier, J. T. Kitasako, and G. I. Hatton. Fractones and other basal laminae in the hypothalamus. *The Journal of Comparative Neurology*, 455(3):324–340, 2003. ISSN 1096-9861. doi: 10.1002/cne.10496. URL `http://dx.doi.org/10.1002/cne.10496`.

Nakamura, A., A. Lindenmayer, and K. Aizawa. *The Book of L.* Springer, Berlin, 1986.

S. Osher and R. Fedkiw. *Level Set Methods and Dynamic Implicit Surfaces.* Springer, New York, 2003.

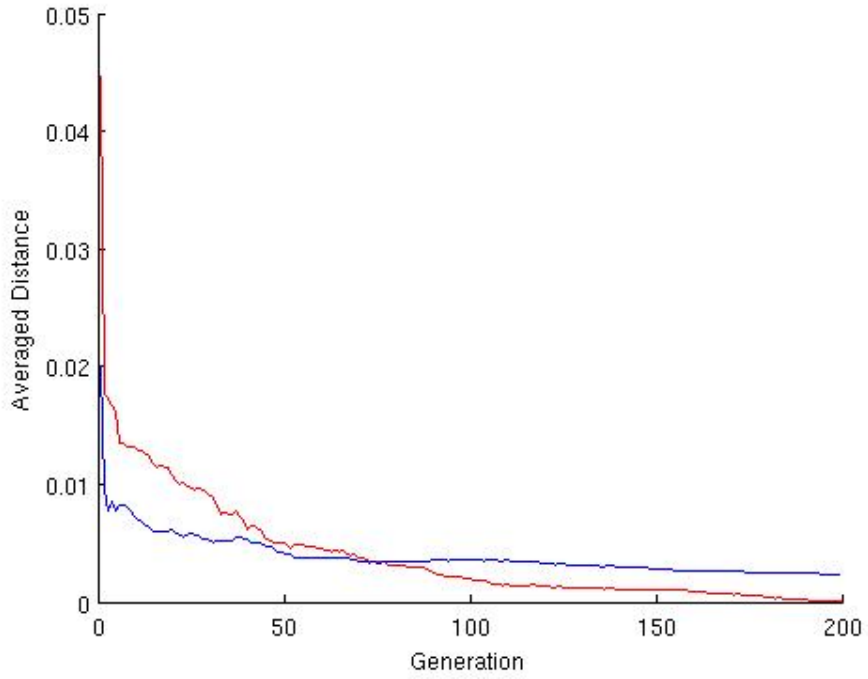

Figure 25: Averaged convergence rates for 10 runs: fractone mapping in red, original mapping in blue

P. Prusinkiewicz and A. Lindenmayer. *The Algorithmic Beauty of Plants*. Springer, New York, 2004.

G. Rozvany. *Topology optimization in structural mechanics*. Springer–Verlag, Berlin, 1994.

B. Stanford, P. Beran, and M. Kobayashi. Aeroelastic optimization of flapping wing venation: A cellular division approach. *AIAA journal*, 50(4):938–951, 2012.

B. K. Stanford, P. S. Beran, and M. H. Kobayashi. Aeroelastic optimization of flapping wing venation: a cellular division approach. 52nd AIAA/ASME/ASCE/AHS/ASC Structures, Structural Dynamics and Materials Conference, Denver, Colorado, 2011.

N. P. van Dijk, K. Maute, M. Langelaar, and F. van Keulen. Level-set methods for structural topology optimization: a review. *Structural and Multidisciplinary Optimization*, 48:437–472, 2013. doi: 10.1007/s00158-013-0912-y.

C. Wang, Z. Zhao, M. Zhou, O. Sigmund, and X. S. Zhang. A comprehensive review of educational articles on structural and multidisciplinary optimization. *Structural and Multidisciplinary Optimization*, 64:2827–2880, 2021.